2007-03-21

Particle Size, Gas Temperature, and Impingement Cooling Effects on High Pressure Turbine Deposition in Land Based Gas Turbines from Various Synfuels

Jared M. Crosby
Brigham Young University - Provo

PARTICLE SIZE, GAS TEMPERATURE, AND IMPINGEMENT COOLING EFFECTS ON HIGH PRESSURE TURBINE DEPOSITION IN LAND BASED GAS TURBINES FROM VARIOUS SYNFUELS

by

Jared M. Crosby

A thesis submitted to the faculty of

Brigham Young University

in partial fulfillment of the requirements for the degree of

Master of Science

Department of Mechanical Engineering

Brigham Young University

April 2007

BRIGHAM YOUNG UNIVERSITY

GRADUATE COMMITTEE APPROVAL

of a thesis submitted by

Jared M. Crosby

This thesis has been read by each member of the following graduate committee and by majority vote has been found to be satisfactory.

Date	Jeffrey P. Bons, Chair
Date	Thomas H. Fletcher
Date	Matthew R. Jones

BRIGHAM YOUNG UNIVERSITY

As chair of the candidate's graduate committee, I have read the thesis of Jared M. Crosby in its final form and have found that (1) its format, citations, and bibliographical style are consistent and acceptable and fulfill university and department style requirements; (2) its illustrative materials including figures, tables, and charts are in place; and (3) the final manuscript is satisfactory to the graduate committee and is ready for submission to the university library.

Date

Jeffrey P. Bons
Chair, Graduate Committee

Accepted for the Department

Matthew R. Jones
Graduate Coordinator

Accepted for the College

Alan R. Parkinson
Dean, Ira A. Fulton College of Engineering and Technology

ABSTRACT

PARTICLE SIZE, GAS TEMPERATURE, AND IMPINGEMENT COOLING EFFECTS ON HIGH PRESSURE TURBINE DEPOSITION IN LAND BASED GAS TURBINES FROM VARIOUS SYNFUELS

Jared M. Crosby

Department of Mechanical Engineering

Master of Science

Four series of tests were performed in an accelerated deposition test facility to study the independent effects of particle size, gas temperature, and metal temperature on ash deposits from two candidate power turbine synfuels. The facility matches the gas temperature and velocity of modern first stage high pressure turbine vanes while accelerating the deposition process. This is done by matching the net throughput of particulate out of the combustor with that experienced by a modern power turbine. In the first series of tests, four different size particles were studied by seeding a natural-gas combustor with finely-ground coal ash particulate. The entrained ash particles were accelerated to a combustor exit flow Mach number of 0.25 before impinging on a thermal barrier coated (TBC) target button at 1183°C. Particle size was found to have a

significant effect on capture efficiency with larger particles causing considerable TBC spallation during a 4-hour accelerated test. In the second series of tests, different gas temperatures were studied while the facility maintained a constant exit velocity of 170 m/s (Mach=0.23-0.26). Coal ash with a mass mean diameter of 3 μm was used. Particle deposition rate was found to decrease with decreasing gas temperature. The threshold gas temperature for deposition was approximately 960°C. In the third and fourth test series impingement cooling was applied to the backside of the target button to simulate internal vane cooling. Ground coal and petcoke ash particulates were used for the two tests, respectively. Capture efficiency was reduced with increasing mass flow of coolant air. However, at low levels of cooling the deposits attached more tenaciously to the TBC layer. Post exposure analyses of the third and fourth test series (scanning electron microscopy and x-ray spectroscopy) show decreasing deposit thickness with increased cooling levels. Implications for the power generation goal of fuel flexibility are discussed.

ACKNOWLEDGMENTS

This thesis would not have been possible without the guidance, assistance, and support of several people. I would like to thank my advisor, Dr. Jeffrey Bons, for providing me the opportunity to work on such an interesting and challenging project. I would also like to thank the other members of my graduate committee, Drs. Thomas Fletcher and Matthew Jones. Their varied fields of experience and insight were invaluable to understanding and moving forward in this research. I am also grateful for the generous grant from the U.S. Department of Energy that helped this project to reach completion.

I would also like to express my gratitude for the efforts of Ken Forster, Kevin Cole, and the Precision Machining Lab at BYU without whose talents this project would not have been completed. The efforts and assistance of Spencer Grange in making the CAD model of the fixture, Aaron Mason and Scott Lewis in helping to run experiments and take surface roughness measurements, Robert Laycock in helping to run experiments, grinding particulate, and sizing it in the Coulter Counter, and Weiguo Ai in analyzing frontside temperature measurements were instrumental in the successful completion of this thesis.

Finally, I would like to thank my wife Ashley for her love and support throughout the past two challenging years.

TABLE OF CONTENTS

LIST OF TABLES ..... **ix**

LIST OF FIGURES ..... **xi**

NOMENCLATURE ..... **xv**

1 Introduction **1**

1.1 Background 1

1.2 TADF 4

1.3 Thesis Objective 9

2 Experimental Facility **11**

2.1 Original TADF 11

2.2 TADF Modifications 17

2.3 Turbine Blade Samples 25

2.4 Instrumentation 26

2.5 Particulate Preparation 33

3 Particle Size Series Results **39**

3.1 Testing Conditions 39

3.2 Digital Images 41

3.3 Deposition Statistics 44

3.4 Roughness Measurements 46

4 Gas Temperature Series **49**

4.1 Testing Conditions 49

4.2 Digital Images 50
4.3 Deposition Statistics 51
4.4 Roughness Measurements 54
5 Impingement Cooling Series Coal 57
5.1 Testing Conditions 57
5.2 Digital Images 58
5.3 Deposition Statistics 60
5.4 Roughness Measurements 61
5.5 ESEM Analysis 63
6 Impingement Cooling Series Petcoke 69
6.1 Testing Conditions 69
6.2 Digital Images 70
6.3 Deposition Statistics 71
6.4 Roughness Measurements 72
6.5 ESEM Analysis 74
7 Conclusions and Recommendations 77
7.1 Conclusions 77
7.2 Accomplishments/Recommendations 78
8 References 83
Appendix A. Uncertainty Analysis 87

LIST OF TABLES

Table 1-1: Roughness comparisons between accelerated deposits and serviced hardware...7

Table 2-1: Ash particle summary statistics: size, density, and average elemental composition.....35

Table 3-1: Particle size series test conditions using subbituminous coal 41

Table 3-2: Deposition results from particle size test series using subbituminous coal 44

Table 4-1: Gas temperature series test conditions using subbituminous coal 50

Table 4-2: Deposition results from gas temperature test series using subbituminous coal ...52

Table 5-1: Coal impingement cooling series test conditions.....58

Table 5-2: Deposition results from coal impingement cooling series 60

Table 6-1: Petcoke impingement cooling series test conditions.....69

Table 6-2: Deposition results from impingement cooling test series using petcoke 71

Table A-1: Calibration curve fit uncertainty analysis……89

LIST OF FIGURES

Figure 1-1: Surface map of a serviced turbine blade after 25,000 hours of operation (left) and a map of a button after 4 hours in the TADF (right). The area for each is approximately 4mm x 4mm and the vertical scales are approximately the same.....6

Figure 1-2: SEM cross-section from a 16000-hour service blade with a 50-μm metering bar (left) and an accelerated deposit specimen with a 100-μm metering bar (right) 8

Figure 1-3: Comparison of weight percentages of elements found in deposits on a land-based service turbine blade, an aircraft service blade (as reported by Borom et al, 1996), and a TADF-produced accelerated test sample 9

Figure 2-1: Original TADF schematic 12

Figure 2-2: Original TADF 14

Figure 2-3: Modified TADF air lines.....18

Figure 2-4: Modified flame holders 19

Figure 2-5: Modified flame holders in operation (cone removed) 20

Figure 2-6: New particle feed system used in the TADF 21

Figure 2-7: New specimen holder for TADF.....22

Figure 2-8: Modified TADF in operation 23

Figure 2-9: Temperature profile for standard combustor operating conditions.....24

Figure 2-10: Typical pre-test turbine blade button 26

Figure 2-11: Measured spectral response of the SVS285CLCS camera 28

Figure 2-12: Measured frontside and backside temperatures as a function of cooling 31

Figure 2-13: Calculated heat fluxes due to conduction through the coupon and due to backside cooling for a coupon in the TADF at 1183°C at Mach 0.25 (The gray band represents heat flux estimates for 1st stage vanes in a modern gas turbine).....32

Figure 2-14: Particle size distributions for coal and petcoke ash 35

Figure 2-15: ESEM images of smallest (left) and largest (right) size coal particles 37

Figure 3-1: Post test images of coupon subjected to 13 μm particle size 41

Figure 3-2: Micrograph image taken of deposits found on a turbine blade pressure surface (flow direction is from bottom to top) 42

Figure 3-3: Particle size series post-test buttons immediately following shutdown (top) and following cool down to room temperature (bottom) 43

Figure 3-4: Effect of particle size on net capture efficiency 45

Figure 3-5: Approximate location of the four traces used to calculate roughness values 47

Figure 3-6: Roughness measurements for particle size series 47

Figure 4-1: Gas temperature series post-test buttons immediately following shutdown (top) and after cool down to room temperature (bottom) 51

Figure 4-2: Effect of gas temperature on net capture efficiency using subbituminous coal 54

Figure 4-3: Roughness measurements for gas temperature series 55

Figure 5-1: Coal impingement cooling series post-test buttons immediately following shutdown (top) and after cool down to room temperature (bottom) 59

Figure 5-2: Effect of impingement cooling on net capture efficiency 61

Figure 5-3: Roughness measurements for impingement cooling series using subbituminous coal 62

Figure 5-4: Remaining deposit thickness as a function of cooling level 65

Figure 5-5: Typical image series of bottom (left), middle, and top (right) portions of 5.81 g/s coolant test sample 66

Figure 5-6: Elemental comparison of ash, deposit, and penetration for coal impingement cooling series 67

Figure 6-1: Petcoke impingement cooling series post-test buttons immediately following shutdown (top) and after cool down to room temperature (bottom) 70

Figure 6-2: Effect of impingement cooling on net capture efficiency 72

Figure 6-3: Roughness measurements for impingement cooling series using petcoke 73

Figure 6-4: Remaining deposit thickness as a function of cooling level 74

Figure 6-5: Typical image series of bottom (left), middle, and top (right) portions of 3.38 g/s coolant test sample 75

Figure 6-6: Elemental comparison of ash, deposit, and penetration for petcoke impingement cooling series 76

Figure A-1: Mass flow calibration curve fit……...88

NOMENCLATURE

A	cross-sectional area [m^2]
APS	air plasma sprayed
CWF	coal-water fuel
DN	signal from detector
ESEM	environmental scanning electron microscope
ICP-AES	inductively coupled plasma atomic emission spectroscopy
LPT	low pressure turbine
M	Mach number
MMD	mass mean diameter
P	pressure [Pa]
Q	heat removed [kW]
R	gas constant [J/kgK]
Ra	centerline-averaged roughness [μm]
Rt	maximum peak-to-valley roughness [μm]
Rz	mean peak-to-valley roughness [μm]
SEM	scanning electron microscope
T	temperature [K]
TADF	turbine accelerated deposition facility
TBC	thermal barrier coating
TIT	turbine inlet temperature
YSZ	yttrium stabilized zirconium
$\dot{m}$	mass flow rate [kg/s]
ppmw	parts per million by weight
ppmw-hrs	parts per million by weight times number of hours
slpm	standard liters per minute
C_1, C_2	Planck's law constants
C_D	discharge coefficient
C_{exp}	RGB camera calibration constant
C_p	specific heat [kJ/kg-C]
S_w/S	Total wetted surface area to planform area ratio
S_λ	measured spectral response

d_p	particle diameter [m]
v_f	fluid velocity [m/s]
v_p	particle velocity [m/s]
Λ_s	Roughness shape/density parameter (Sigal et al, 1990) [dimensionless]
γ	specific heat ratio
λ	wavelength
μ	dynamic viscosity [N-s/m^2]
ρ	density [kg/m^3]
α_{rms}	rms deviation of surface slope angles
ρ_p	particle density [kg/m^3]
ε_λ	surface emissivity

1 Introduction

1.1 Background

The effects of solid particles ingested into gas turbines are a universal problem shared by both land based and aircraft turbines. Due to the large air flow that gas turbines require, these particles cannot economically be entirely eliminated from the inlet air flow even with the best filtration and clean-up systems. Internal particulate sources include combustion products of fossil fuels, eroded turbomachinery components, and secondary chemical reactions. External particulate sources vary widely depending on operating environment (marine, desert, industrial) and level of filtration (aero engine, remote power microturbine, or large industrial power plant). These contaminants are heated in the combustor and either follow the flow out of the engine or impact against the turbine blades. The primary processes for delivery of particles to the turbine blades are: inertial impaction, turbulent eddy diffusion, Brownian diffusion, and thermophoresis. The dominate delivery mode is determined by particle size ranges, with inertial impaction dominating for diameters larger than a few microns. The contaminants which impact against the turbine components can cause erosion, corrosion, and deposition. These three adverse effects are well documented in the literature. Erosion of blade tips can open up clearance passages and alter blade profiles, reducing engine efficiency. A study

involving sand ingestion through an axial fan showed a 6-10% loss in overall engine efficiency after nine hours of exposure (Ghenaiet et al., 2001). Deposition can clog blade passages, reducing mass flow through the engine, resulting in a loss of power. In addition, deposition can block film cooling holes, resulting in engine failure (Kim et al., 1993). Deposition can also contribute to faster corrosion rates of blades by bringing a high concentration of corrosive elements in contact with engine components. Studies have shown that deposition and erosion increase turbine blade roughness, which can greatly augment convective heat transfer and skin friction (Bons, 2002; Bons et al., 2006). Erosion and deposition are competing phenomena and depend on the phase of the particulate impacting the blade surfaces. While there are numerous secondary parameters influencing these processes, generally the particulate erodes the blades when it is below the softening temperature, and adheres to the blades when above the softening temperature. This threshold temperature depends on the particulate type, but has been shown to occur between 980 and 1150°C (Wenglarz & Wright, 2002; Smialek et al., 1992; Toriz et al., 1988; Wenglarz & Fox, 1990; Kim et al., 1993).

The primary factors affecting the extent of deposition on turbine blades include: gas temperature, turbine surface temperature, net particle loading, particulate chemical composition, turbine blade exposure time, and geometric boundaries imposed on the flow. Previous turbine tests with coal-derived fuels by Wenglarz and Fox (1990) show a dramatic increase in deposition rate as the gas temperature is raised above the particulate melting point. In their study, coated turbine superalloy specimens were subjected to 2-5 hours of deposition from three coal-water fuel (CWF) formulations. The coal had been cleaned to simulate ash levels (~1 wt%) that would be considered acceptable for use in a

gas turbine. The fuel was burned in a low-emission subscale turbine combustor at realistic flow rates (e.g. impact velocities ~ 180 m/s) and gas temperatures (1100°C). With the turbine specimens located at two different streamwise locations downstream of the combustor exit, the influence of gas temperature on deposition rate could be studied. It was noted that the upstream specimens (operating at gas temperatures ~ 1100°C) experienced 1 to 2 orders of magnitude higher deposition rates compared to the downstream specimens (operating at gas temperatures ~ 980°C). Compared to a previous series of tests with lower ash content residual fuel oil (0.025 wt%), the deposit levels with coal-water fuels were 2 to 3 orders of magnitude larger for the same operating temperature. An aero-engine deposition study performed by Kim et al. (1993) with volcanic ash showed that the rate at which deposition occurs increases with time for a given turbine inlet temperature (TIT) and dust concentration, i.e., the vanes become better captors of material as the deposits on the vanes increase. It was also found that once deposition begins, the mass of material deposited is proportional to dust concentration for a given TIT and dust exposure time.

Wenglarz and Fox (1990) also explored the possibility of sub-cooling the upstream turbine specimens and found a factor of 2.5 reduction in deposits for a 200°C drop in metal surface temperature. Lower deposit formation in areas of reduced surface temperature was also noted by Bons et al. (2001) in their study of serviced turbine hardware. Cooled turbine vanes which exhibited large (1-2 mm thick) marine deposits over their entire surface were noticeably free of deposits in the film cooling flow path where surface temperatures are significantly lower. This effect created substantial troughs or “furrows” which extended for more than 10 hole diameters downstream of the

cooling hole exit. These results confirm the important role of gas and surface temperature in determining deposition rates from ash-bearing fuels.

Due to current economic and political pressures, alternate fuels such as coal, petcoke, and biomass are being considered to produce substitute syngas fuels to replace natural gas in power turbines. Given the present volatility in natural gas markets and the uncertainty regarding projected fuel availability over the 20-30 year design lifetime of newly commissioned power plants, coal and petroleum derivative fuels are already being used at a handful of gas turbine power plants worldwide. In addition, intermediate goals of the DOE Future Gen and DOE Turbine Program focus on coal syngas as a turbine fuel in an effort to reduce dependency on foreign supplies of natural gas. Thus, the stage is set for broader integration of alternate fuels in gas turbine power plants. Studies of potential sources of deposition from these syngas fuels are necessary so that their adverse effects can be minimized. Deposition has numerous adverse results that can range from decreased engine performance to catastrophic failure. For monetary as well as safety reasons, it is highly desirable to reduce or eliminate these effects.

1.2 TADF

In all but the most severe conditions, deposition is a relatively slow process and its study on an actual turbine is neither time nor cost efficient. To remedy this, the Turbine Accelerated Deposition Facility (TADF) was developed in 2004 which simulates 8,000 hours (1 year) of exposure time in a real gas turbine engine in a four hour test. This is done by matching the net particle throughput mass at realistic combustor gas exit temperatures and velocities. The construction of the TADF and the validation of this

hypothesis was the subject of a thesis by Jensen (2004). In his thesis, Jensen compared accelerated deposits from airborne particulate to those found on serviced hardware. Because the validation of the TADF is covered in detail by Jensen (2004), Jensen et al. (2005), and Wammack (2005), only a terse treatment of the validation of the TADF will be given.

Jensen validated the TADF by comparing specific features from accelerated deposition buttons to deposit features found on in-service hardware. The criterion used for determining whether the two modes of deposition were indeed similar was based upon thermodynamic considerations. Deposits alter the blade thermodynamics through two primary mechanisms: convection and conduction. Convection is influenced by changes in surface roughness. Bons (2002) tested scaled models of actual turbine deposit roughness and found 20-40% increases in convective heat transfer. Several roughness statistics were suggested as possible correlating parameters for the observed increase in heat transfer. Thus, Jensen proposed that if the deposits generated in the accelerated deposition facility have a statistically similar character to those found on actual in-service hardware, they would be considered "similar". Accordingly, surface topology measurements were made to allow statistical comparisons of roughness.

Deposits also form an insulating layer over the TBC, thus reducing heat flow to the metal substrate. This conduction mechanism is governed by the deposit thickness, chemistry, and structure. As such, measurements were made of the deposit internal structure and chemical composition using a scanning electron microscope (SEM) and x-ray spectroscopy. The results of these two studies are presented below.

Surface roughness in turbines is governed by a variety of parameters including: service hours, cycles, operating temperature, and environment. Bons et al (2001) reported significant variations with blade location and surface degradation mechanism (spallation, deposition, or erosion) as well. Because of these various parameters, Jensen (2004) did not expect to match a specific surface topology from a serviced turbine to that obtained in the TADF. Instead, statistical comparisons were used to show that surface formations have similar character and thus would influence performance (e.g. convective heat transfer) in a similar way. The surface of a button subjected to a 4 hour test in the TADF with a particulate loading of 60 parts per million by weight (ppmw) (see Chapter 2.1 for information regarding particulate loadings), as well as the surface of a serviced turbine blade that had 25,000 hours of operation, were scanned using a profilometer to determine the roughness of their surfaces as well as to produce three-dimensional surface maps as shown in Figure 1-1.

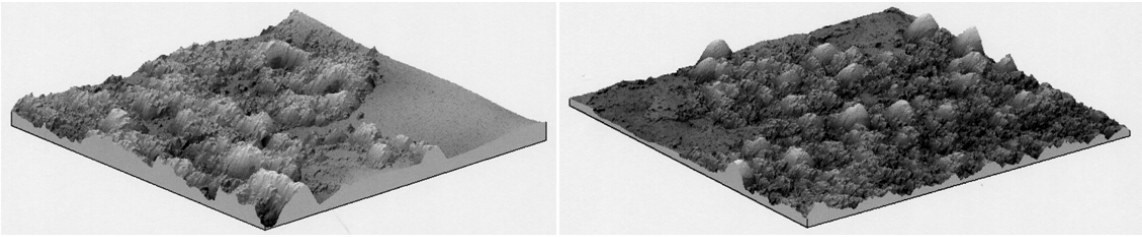

Figure 1-1: Surface map of a serviced turbine blade after 25,000 hours of operation (left) and a map of a button after 4 hours in the TADF (right). The area for each is approximately 4mm x 4mm and the vertical scales are approximately the same

Although there are some visible differences between the above two surfaces—most notably that the accelerated deposit's surface is dominated by more distinct peaks than that of the serviced turbine blade—the respective heights of the roughness features

are of the same order of magnitude. The surface roughness statistics shown in Table 1-1 reinforce the strong similarities between the accelerated deposits and the serviced hardware. Though there are wide ranges of statistics for both the accelerated and serviced deposits, the ranges overlap noticeably. Thus, from a convective heat transfer standpoint, Jensen (2004) concluded that the accelerated deposits were considered "similar" to those found in actual serviced hardware.

Table 1-1: Roughness comparisons between accelerated deposits and serviced hardware

	Surface Type	Ra (μm)	Rt (μm)	α_{rms}	S_w/S	Λ_s
Accelerated Test (4 hours)	60ppmw, at coupon edge	28	257	29	1.43	13
	280ppmw, 90deg impingement	32	260	16.5	1.12	82
	280ppmw, 45deg impingement	10	107	13.7	1.06	180
	280ppmw, at coupon edge	38	249	18	1.11	87
Serviced Blades	25000hr blade	32	240	27	1.36	22
	22500hr blade	41	296	24	1.24	36
	<1000hr blade	19	394	18	1.11	77
	24000hr vane	17	220	15.8	1.09	134

In addition to increasing the rate of convective heat transfer between the exhaust gases and the surface of the deposits, deposits tend to form an insulating layer; their second thermodynamic effect on a turbine blade. Given the difficulty in accurately measuring the thermal conductivity of deposit layers, Jensen (2004) studied extensively two factors which strongly affect overall thermal conductivity: deposit structure and chemical composition. Internal structure and chemical composition were compared by cross-sectioning the samples and the serviced blades and then looking at them in a SEM.

A comparable internal structure was found to exist between the two deposits (Figure 1-2). Both deposits showed elongated structures which ran parallel to the turbine blade surface. The 100 μm thick accelerated sample shown on the right is of the same order of magnitude in size as actual turbine blade deposits shown on the left. Other microstructures including pitting and grain sintering were also observed in both turbine blade and accelerated specimen cross-sections.

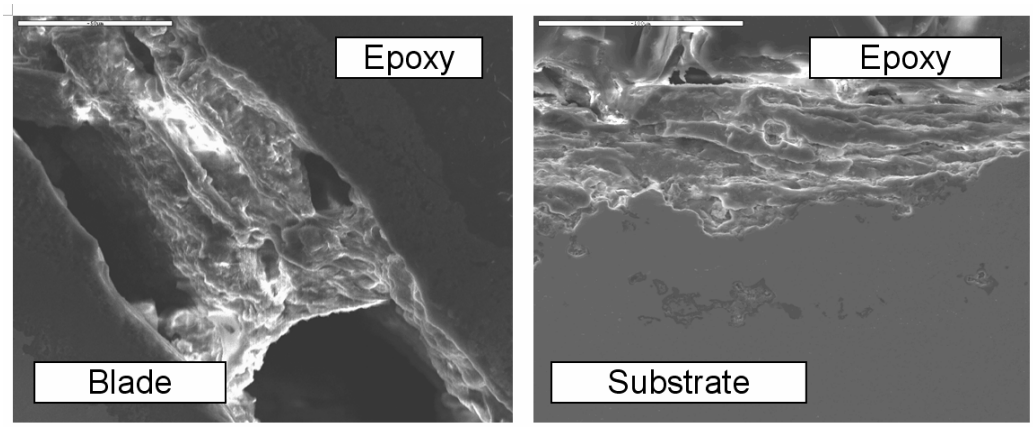

Figure 1-2: SEM cross-section from a 16000-hour service blade with a 50-μm metering bar (left) and an accelerated deposit specimen with a 100-μm metering bar (right)

The SEM was also used to perform x-ray spectroscopy to identify the elemental composition of the accelerated deposit produced in the TADF as well as that of the serviced blade. Both compositions were compared to a study performed by Borom et al. (1996) in which deposition on an aircraft engine blade exposed to desert conditions was reported. As shown in Figure 1-3, the chemical composition of the accelerated deposits most closely matched the composition of the deposits studied by Borom et al. Some variation was expected, however, due to the variety of chemical mixtures that can be found in different environments. Most importantly, Jensen's analysis of several locations

throughout the accelerated deposit layer showed that, like in-service turbine blades, the distribution of the component chemicals throughout the accelerated deposits was relatively homogeneous. This comparison, combined with the internal structure evaluation, suggested that similar heat conduction paths exist between deposits from serviced blades and deposits formed in the TADF.

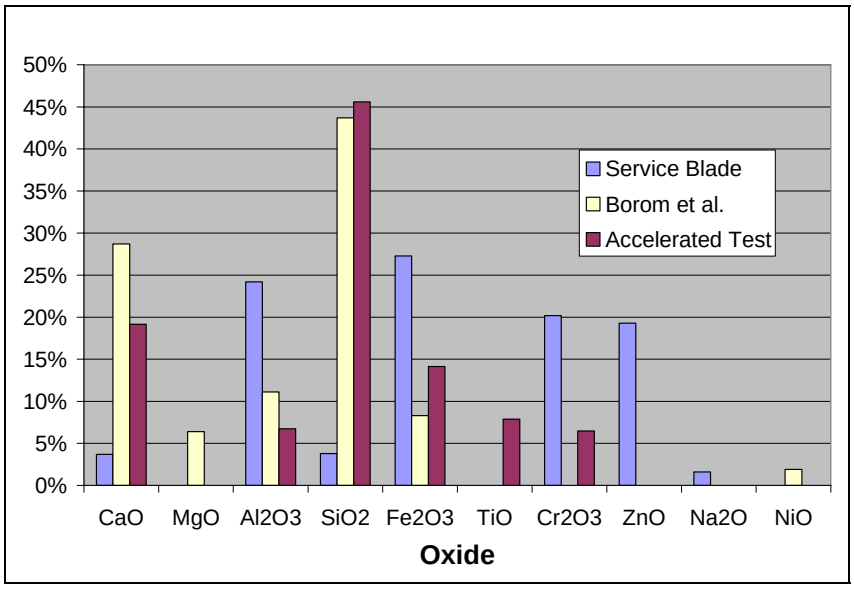

Figure 1-3: Comparison of weight percentages of elements found in deposits on a land-based service turbine blade, an aircraft service blade (as reported by Borom et al, 1996), and a TADF-produced accelerated test sample

1.3 Thesis Objective

Since its construction and validation, the TADF has been used in a number of studies. One study involved alternate fuel deposition from coal, petcoke, and biomass (straw and sawdust) at constant operating conditions (Bons et al., 2007). Surface roughness of the different deposits, as well as deposit elemental composition, was

compared. Another study involved the evolution of deposits with repeated exposure (Wammack et al., 2006; Bons et al., 2006). Roughness evolution was measured in successive simulations of three month operating periods. Scaled models of the deposit surfaces were made and used in wind tunnel experiments to determine the change in convective heat transfer coefficient over time. However, all of the previous studies performed using the TADF have been at nearly isothermal conditions. In other words the turbine blade samples had approximately no temperature gradient across them. In order to maximize engine efficiency, modern gas turbine engines employ high temperature alloys, ceramic coatings, and internal as well as film cooling to protect the turbine section, which allows for higher operating temperatures. The internal cooling results in substantial temperature gradients across the turbine blades, while film cooling produces a thin protective film of air on the exposed surface of the blade. The objective of the present thesis is twofold. The first is to create more realistic engine conditions by modifying the TADF in such a way as to produce a similar thermal gradient to those found in modern turbines through the use of impingement cooling on the backside of the turbine blade sample, while also allowing for future implementation of film cooling. The second objective is to use this modified facility to characterize the effects of deposition from alternate fuels on turbine blade materials, independently varying the particle size, gas temperature, and backside cooling level.

2 Experimental Facility

2.1 Original TADF

The TADF was originally built in 2004. A schematic of the TADF is shown in Figure 2-1. It is essentially a partially premixed natural gas burning combustor capable of steady state operation at volumetric flow rates up to 1000 slpm. The main air enters the base of the combustor and is diffused by 1.3 cm diameter marbles, which distribute the air evenly around the base. The air is then straightened through an aluminum honeycomb section before combusting with partially premixed natural gas which enters through four curved tubes. The exit contraction changes from 30.5 cm to 1.6 cm, which allows the exit flow from the combustor to reach velocities as high as 350 m/s depending on the mass flow rate. A specimen holder is positioned approximately 2-3 jet diameters from the combustor exit and is used to expose 1" diameter turbine material buttons to the hot exhaust gases at several possible impingement angles (30, 45, 60, and 90°). Because particulate deposition occurs through various modes depending on the size of the particulate in the exhaust gases, adjusting the impingement angle helps to properly simulate engine conditions.

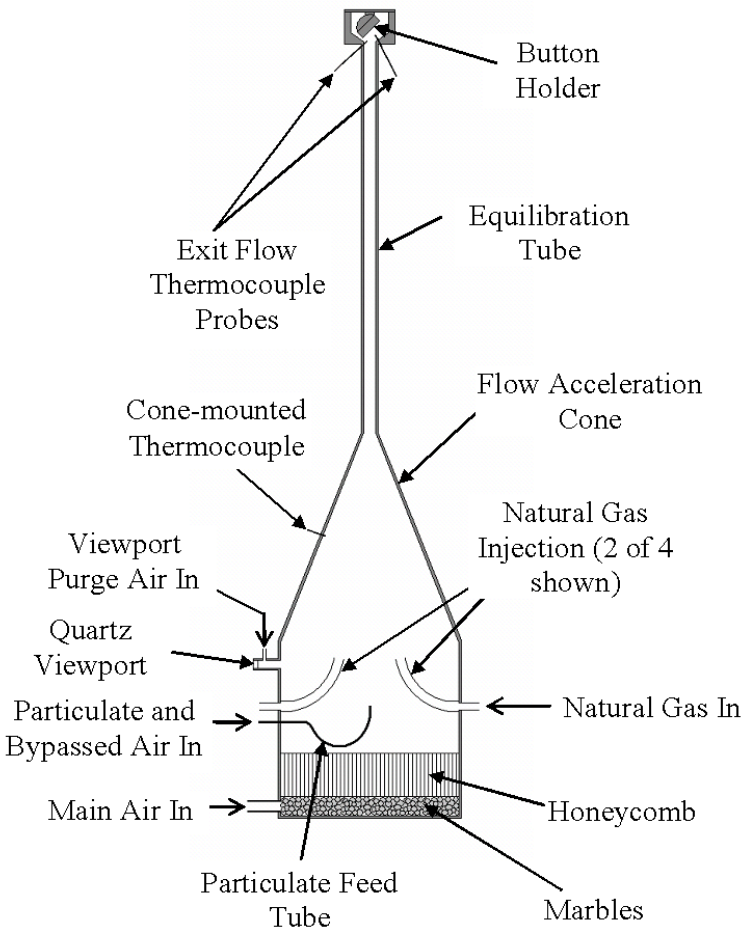

Figure 2-1: Original TADF schematic

The entire hot section of the combustor is manufactured from Inconel 601 which is capable of operating at temperatures as high as 1250°C. A water-cooled hood collects the exhaust gases and cools them before releasing them into the atmosphere. Since the combustor operates using methane and filtered high pressure air, deposits are created by seeding the combustor with the selected particulate of interest using a separate particle feed system. The feeder consists of a motor driven syringe and glass bulb which allows controlled rates of fine, dry particulates to be added into the base of the combustor through a secondary air line. The equilibration tube is approximately 1 m in length and

ensures that the entrained particles are brought up to 95% of the flow velocity and temperature before impacting on the turbine material. The length of this tube was dictated by the estimated residence time required for particles of up to 40 μm in diameter to come to thermal and velocity equilibrium with the gas flow at the nominal test conditions. Jensen (2004) calculated that thermal equilibrium (analyzed using a lumped capacitance model) was achieved for all particles (up to 80 μm) in about 20% of the time required for velocity equilibrium however, large particles would not achieve velocity equilibrium (defined as 95% of gas velocity) before impingement. By applying the Stokes Flow assumptions (assuming spherical particles) on viscous flow, the entrainment of particles in this facility was modeled using Eq 2.1.

$$\rho_p \frac{\pi}{6} d_p^3 \frac{dv_p}{dt} = 3\pi\mu d_p \left(v_f - v_p\right) \tag{2.1}$$

This equation predicts that particles larger than approximately 40 μm will not achieve the full 95% of flow velocity to be considered entrained with the flow.

The combustor's original base operating conditions were an exit velocity of 220 m/s (Mach 0.3) and an exit temperature of 1150°C, thus simulating the conditions at the entrance of a typical first stage nozzle guide vane for an F-class power generation turbine. One flow parameter that is not simulated is static pressure (deposition occurs at approximately atmospheric conditions). Jensen et al. (2005) site a number of sources for facilities that also operate at lower pressures than an operating gas turbine engine and all concluded that particle temperature, concentration, and residence time are the critical

parameters for proper simulation rather than static pressure. The original TADF as designed in 2004 is shown in Figure 2-2.

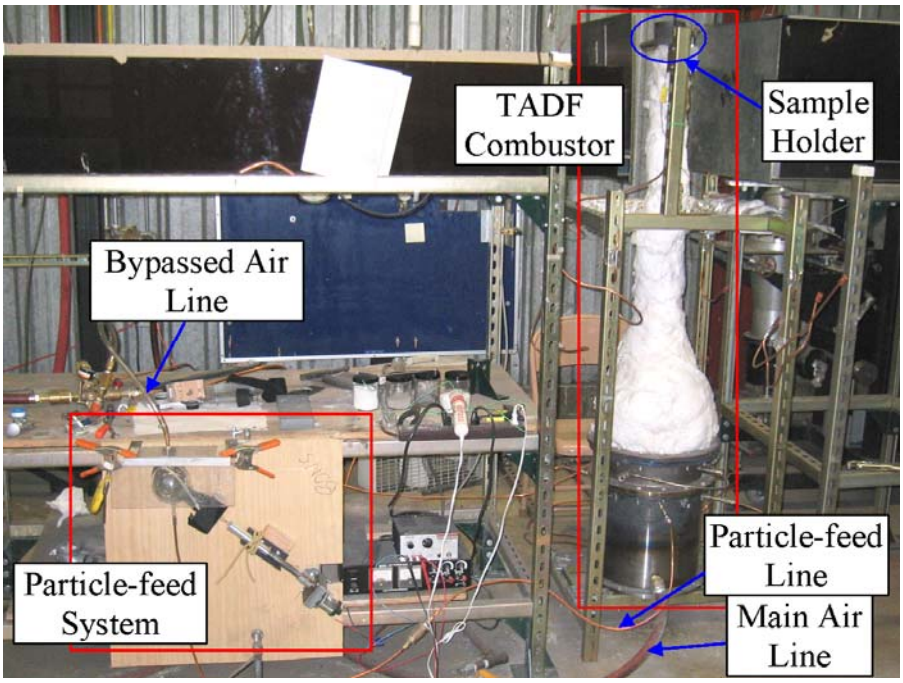

Figure 2-2: Original TADF

Particle concentration is the final major parameter in an operating gas turbine engine that is matched by the TADF. The key feature of the TADF, as mentioned in Chapter 1, is that it can simulate 8000 hrs (1 year) of a turbine's operation in a four hour test. Wenglarz and Wright (2002) describe a number of studies conducted where particulate concentration and service time seemed to trade off with one another. Turbines experienced large deposits or in some cases were even driven to failure by either high particle loading at short service times or low particle loading for long service times. Their work suggested that the net particulate throughput is a key parameter for proper deposit simulation. Thus the time needed to produce deposit can be reduced considerably

by increasing the concentration of particulate. There are of course limits to this theory. The void fraction, defined as the volumetric flow rate of the gas divided by the sum of the volumetric flow rates of the gas and the particles, is a common metric used to characterize when particle interactions become significant. Smoot and Pratt (1979) state that for pulverized coal combustion the void fraction must be greater than 0.99 (or one minus the void fraction must be less than 0.01) to neglect particle interactions. For the highest volumetric flow rate of particles used in this study, one minus the void fraction was calculated to be $2.72e^{-9}$. Thus the bulk density (mass of the gas per unit volume of gas-particle mixture) can be represented by the gas density, to a good approximation.

As mentioned previously in Chapter 1, the hypothesis that deposits could be formed by decreasing the operational time and increasing the particle concentration was verified by Jensen (2004) using airborne particulate. Jensen compared various four hour tests run at particle concentrations between 60-280 ppmw to serviced blades that had seen 22,000-25,000 hrs of operation. The principle behind the production of accelerated deposits is that of matching the product of the particle flow rate and the number of hours of operation. Thus, if the particle flow rate through a gas turbine and the number of hours of operation was known, then the particle flow rate through the TADF could be determined for a given experimental time period. The Department of Energy has set 0.01-0.02 ppmw as a goal for particle concentration seen in an operating gas turbine engine over 8000 hrs (1 year) of operation. Multiplying the particle concentration by the number of operating hours yields a net particulate throughput metric termed “ppmw-hrs”. Dividing the ppmw-hrs by the number of hours in the desired accelerated deposition test dictates what the particle concentration should be in the TADF. A similar metric was

used by Caguiat (2002) and Syverud (2005) in their studies of accelerated compressor fouling caused by salt water ingestion. Because this is the premise upon which the TADF operates an example calculation is shown below (Eqs 2.2-2.4). There are obvious limits to this equation. The test time cannot be reduced to zero. Jensen (2004) compared serviced hardware, which would represent the longest test time and the lowest particle concentration at which the TADF could be operated (which would defeat its purpose), and accelerated tests of four hours and particle concentrations of 60-280 ppmw. Since all of the tests presented in this work were 4-5 hours and at particle loadings from 18-33 ppmw the results lie well within the range at which the TADF was validated. To date the lower limit (shortest test time at highest loading) for which this linear relationship of ppmw-hrs would still hold has not been studied.

Engine Particle Flow (ppmw) x Operational Hours =

TADF Particle Flow (ppmw) x Experiment Hours (2.2)

Thus

TADF Particle Flow (ppmw) = Engine Particle Flow (ppmw) x Operational Hours / Experiment Hours (2.3)

20-40 ppmw = (0.01-0.02 ppmw) x (8000 hrs) / (4 hrs) (2.4)

2.2 TADF Modifications

As mentioned in Chapter 1, modern engines employ significant internal and film cooling schemes to help protect turbine blade materials. In order to more closely model these conditions, significant modifications were made to the TADF. The first modification involved a complete redesign of the combustor air supply line. In its original design the high pressure combustor air (supplied from a compressor) was controlled by an actuated valve located upstream of a choked orifice plate. The valve controlled the mass flow rate in the combustor and was controlled by a power supply which, in order to maintain a constant flow rate (and thus exit velocity), had to be manually adjusted throughout the duration of a test because of supply fluctuations from the compressor. This was a tedious process and took the full attention of one operator which usually meant that two operators needed to be present during the entire duration of a test. The valve was eliminated and the choked flow orifice plate was moved closer to the combustor. The air supply line was branched into two separate lines, one for the combustor flow and one for the coolant flow. A second orifice plate was installed on the coolant line. Air regulators were incorporated upstream of both orifice plates to eliminate the compressor supply fluctuations (and the need for constant manual adjustment) and allow for adjustment of the combustor and coolant air independently. Figure 2-3 shows the modified air lines with their various components. Pressure transducers and thermocouples mounted just upstream of the orifice plates allow for the combustor and coolant mass flows to be measured and monitored by applying Eq. 2.5, the choked flow orifice equation. The discharge coefficient (C_D) was found through calibration using a mass flow meter (see Appendix A for mass flow uncertainties).

$$\dot{m} = \frac{C_D A P}{\sqrt{RT}} \sqrt{\gamma} \left(\frac{2}{\gamma + 1} \right)^{\frac{\gamma+1}{2(\gamma-1)}} \tag{2.5}$$

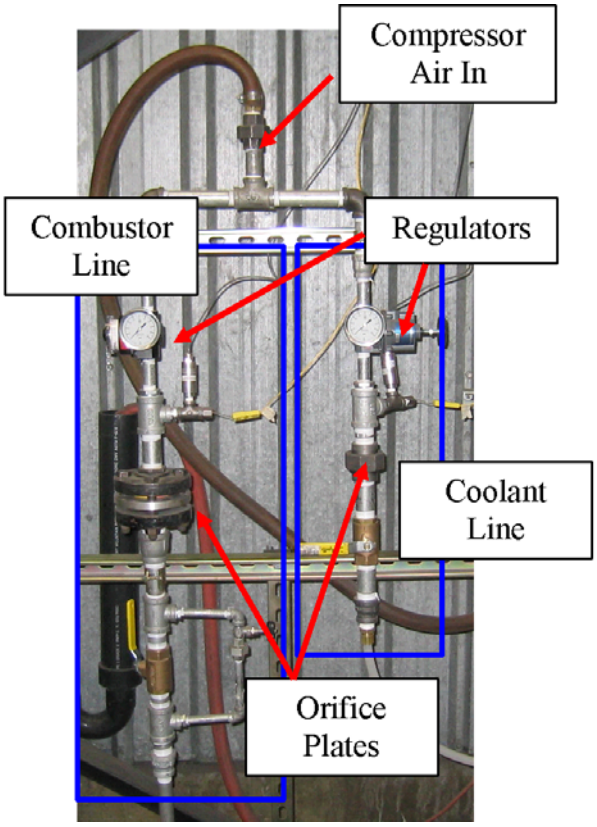

Figure 2-3: Modified TADF air lines

The next modification involved the combustor itself. Because of a number of previous failures of the equilibration tube during testing it was determined (for safety reasons) to increase the tube's inner diameter from 1.6 cm to 2.6 cm (or approximately 1 inch) to prevent failure of the tube and at the same time allow for better particulate exposure of the 1" diameter turbine buttons used in testing. The larger diameter was also desired to provide a more uniform temperature profile. The increase in the tube's

diameter required an increase in the combustor air mass flow in order to maintain the desired exit velocity. A corresponding increase in methane was also required to maintain the appropriate exit temperature.

Initial tests indicated flame stability problems as a result of the increased mass flows. In an attempt to solve this problem, the number of natural gas inlet tubes was doubled from 4 to 8, and small slots were cut into the tips of the tubes to help anchor the flames to the flame holders. With these modifications the combustor was still unable to reach the previous operating exit velocity of 220 m/s (Mach 0.3) with a stable flame at 1150°C. The highest stable operating condition (at 1150°C) reached was slightly lower at approximately 183 m/s (Mach 0.25), but still in the range of typical operating F-class engines (see Appendix A for velocity and Mach uncertainty). Figure 2-4 shows the modified flame holders and Figure 2-5 shows the achievement of a stable flame at higher mass flows.

Figure 2-4: Modified flame holders

Figure 2-5: Modified flame holders in operation (cone removed)

Another important modification made to the TADF was the implementation of a new particle feed system. The previous system was erratic and proved to have major repeatability problems. Because the amount of particulate injected into the combustor is such a crucial parameter for accelerated deposition, an improved system was developed. The use of a motor driven syringe was still employed as previously, however the bulb into which the syringe emptied was changed. The motor which drives the syringe was connected to a function generator to allow for greater control of the speed at which it pushes the syringe. A separate motor was connected to a brush and placed inside the bulb to help break up the particulate as it leaves the syringe. Vibration is also used to keep particulate from adhering to the inside of the bulb. Bypassed air enters through the top of the bulb and is forced out through the bottom on its way to the combustor. The new particle feed system is shown in Figure 2-6. Testing was conducted to determine the frequency of the motor needed to feed the proper amount of particulate into the

combustor. This testing showed the new particle feed system to be a vast improvement over the previous one in terms of repeatability as well as reliability. This improvement was evident in the four test series conducted. For example, in one of the test series studied, six tests were performed at a desired particle concentration of 24 ppmw with less than 12% variation. In another test series four tests were performed at a desired particle concentration of 22 ppmw with less than 9% variation.

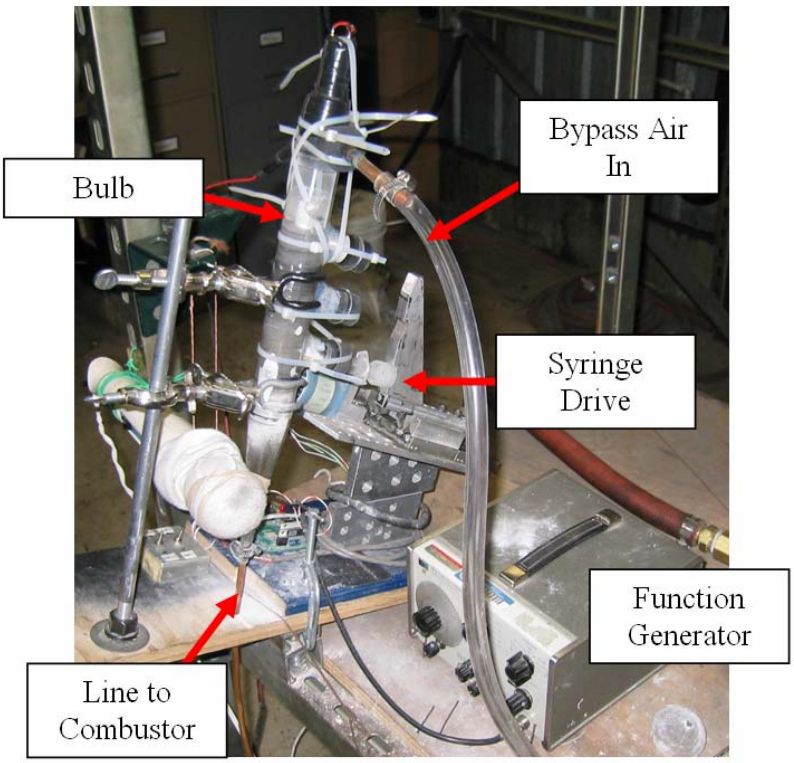

Figure 2-6: New particle feed system used in the TADF

The final modification to the TADF was the largest and most important. The sample holder at the top of the equilibration tube was removed and a completely new specimen holder was designed to allow for backside impingement cooling of the turbine blade sample. The new specimen holder is shown in Figure 2-7. Cool air is brought in

through the center tube, impinges on the back side of the sample, and exits through the outer tube. The entire fixture is insulated with ceramic batting to minimize 3-D heat transfer losses and is positioned within one jet diameter of the equilibration tube exit.

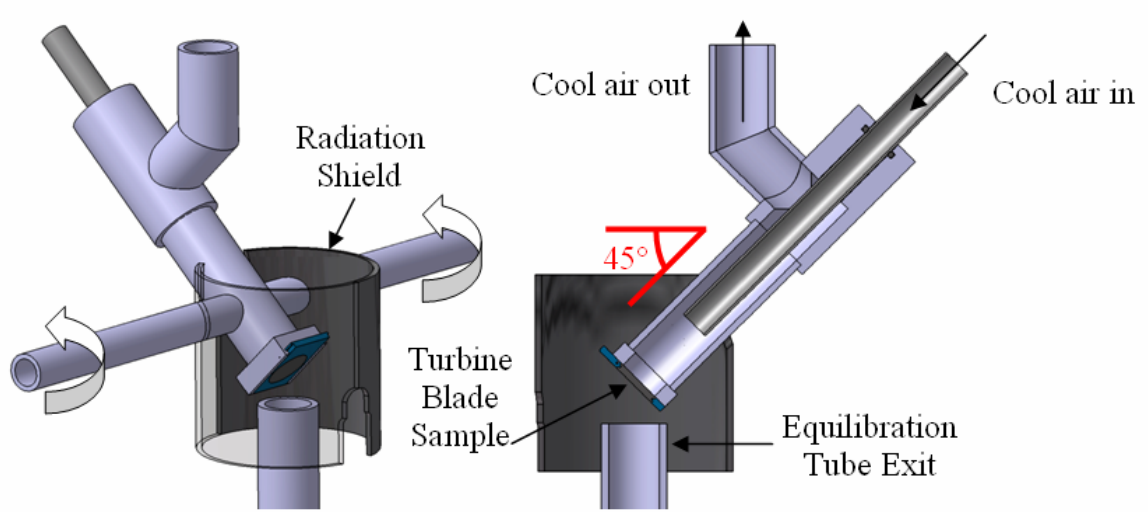

Figure 2-7: New specimen holder for TADF

When impingement cooling is used, the backside temperature of the sample is measured using two welded K-type thermocouples. Inlet and exit coolant temperatures are measured using K-type thermocouples as well. The sample's frontside temperature is measured using an RGB camera through a technique that will be described later. A radiation shield helps minimize radiative losses while also providing optical access through a cutout for the RGB camera as well as digital video recording. The specimen holder can be rotated to hold the turbine sample at any impingement angle. All the tests in this thesis are conducted at 45° as shown in Figure 2-7, since this is representative of the leading edge stagnation region of a first stage vane. This impingement angle was found to produce the maximum surface degradation in tests conducted by Jensen et al.

(2005) over a range of angles from 30 to 90º. The modified TADF is shown in operation in Figure 2-8.

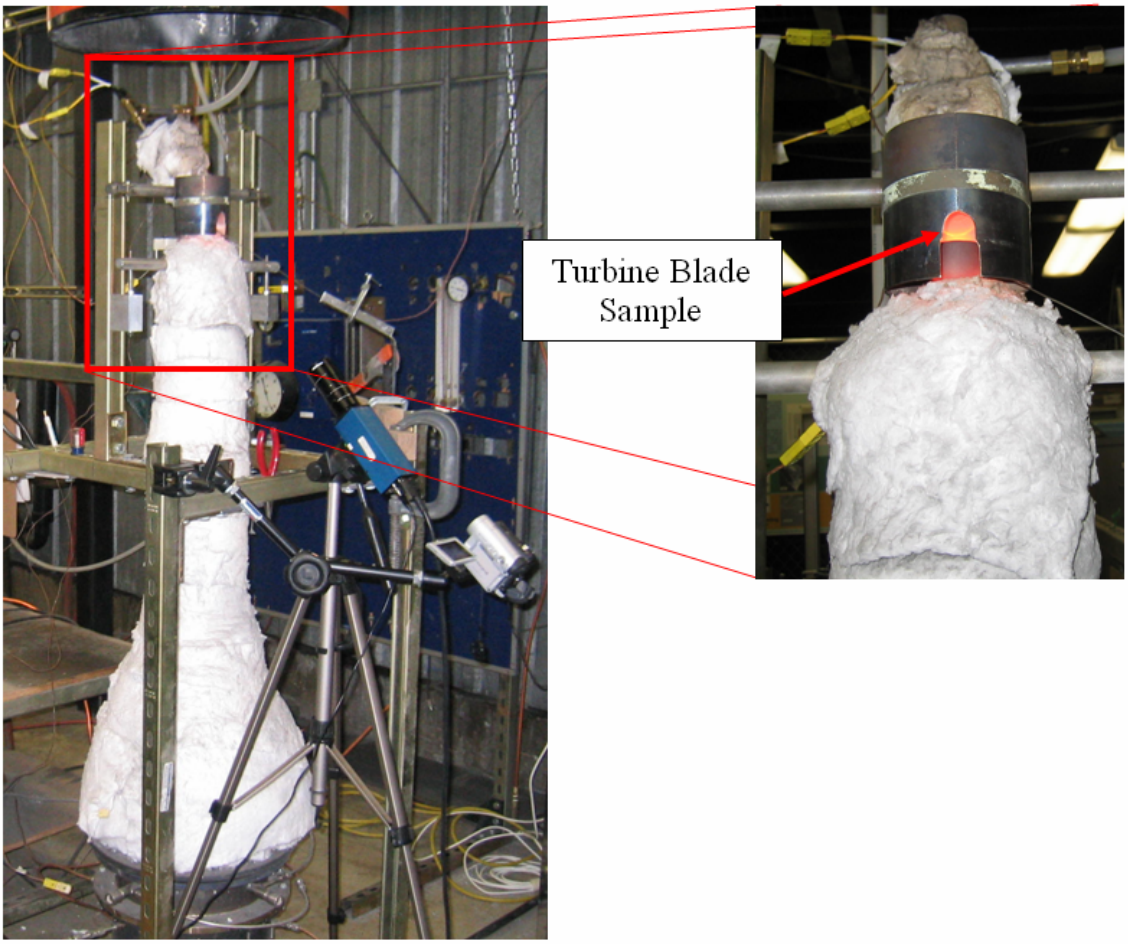

Figure 2-8: Modified TADF in operation

With all the modifications completed, new standard operating conditions were established. The original operating conditions, as mentioned previously, could not be obtained. However, it was still desirable to achieve the same exit temperature (1150ºC) and remain in the range of typical exit Mach numbers for first-stage turbine blade rows (0.2-0.4). Primary combustor air mass flow through the choked flow orifice plate was

measured at 0.0214 kg/s with an uncertainty of ±4.7% (see Appendix A). This was the highest mass flow attainable before flame stability problems developed. This mass flow and an exit temperature of 1150ºC produced an exit Mach number of 0.25 with an uncertainty of ±8.5% (see Appendix A). The exit temperature profile was measured by traversing a high temperature K-type thermocouple probe across the lip of the equilibration tube exit. The thermocouple was not shielded, and a radiation correction of 33°C at 1150°C was estimated using an emissivity of 0.5 for the oxidized Omegaclad™ probe surface. Figure 2-9 shows the exit temperature profile at standard operating conditions (gas exit temperature = 1183°C with radiation correction, Mach = 0.25).

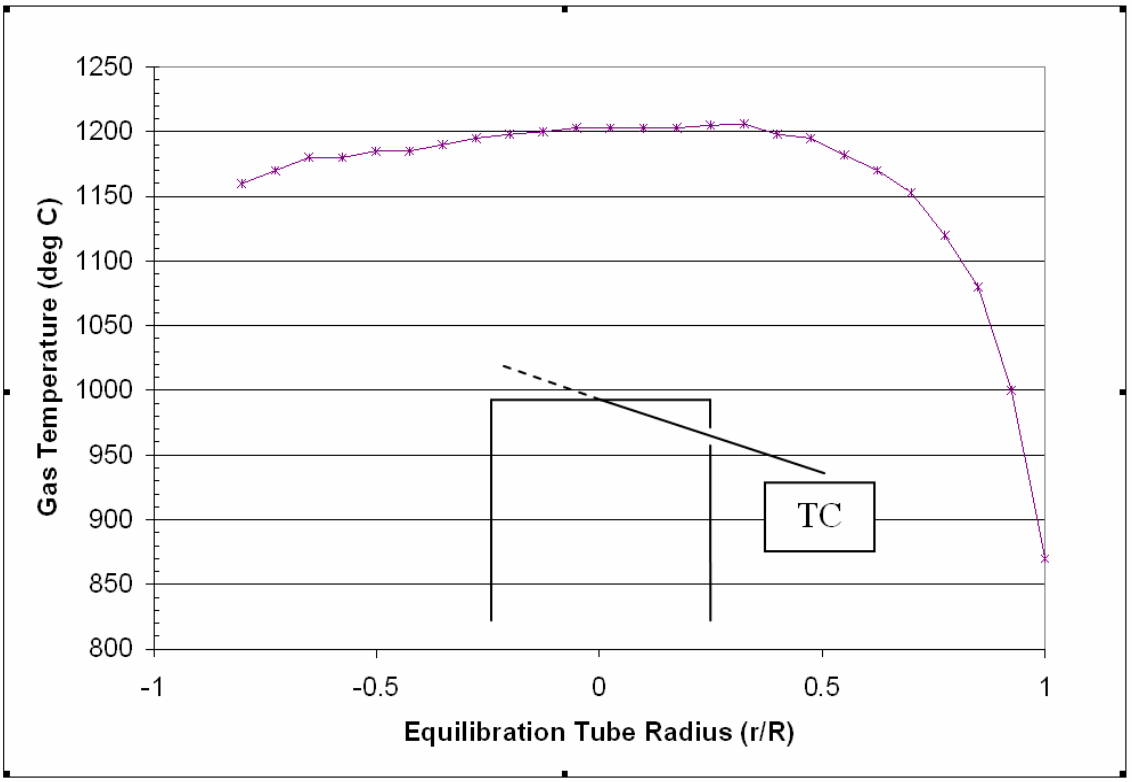

Figure 2-9: Temperature profile for standard combustor operating conditions

The schematic in Figure 2-9 shows the approximate path which the thermocouple traversed while taking the measurements. The temperature began to drop beyond the center of the tube as the thermocouple moved further from the exit of the equilibration tube. Except where otherwise stated, all tests in this thesis are conducted at these standard operating conditions. For all tests the combustor is brought to steady state operating conditions before particle feeding commences. All tests times indicated refer to the number of hours in which particulate is seeded into the combustor.

2.3 Turbine Blade Samples

Three sets of circular turbine blade samples, all approximately 2.54 cm (1 inch) in diameter, were obtained from multiple industry sources for the tests performed in this study. In order to respect proprietary concerns of the manufacturers, strict source anonymity has been maintained for all data presented in this publication. The samples are representative of a high performance turbine material system: a nickel based super alloy substrate approximately 0.3 cm thick was common to all three sets, an MCrAlY bond coating approximately 225 μm thick for the first set, 200 μm for the second, and 175 μm for the third, and an air plasma sprayed (APS) yttrium stabilized zirconium (YSZ) thermal barrier coating (TBC) layer approximately 0.45 mm thick for the first set, 0.40 mm for the second, and 0.17 mm for the third. The samples were polished to a centerline-averaged roughness (Ra) value of 1-1.5 μm. Each of the three sets of buttons was used for a different test series, as will be explained in the results section, therefore consistency for each test series was maintained. A small groove was machined around the circumference of each sample to allow it to be held in the cooling fixture with

adequate sealing to contain the coolant. A typical pre-test button is shown in Figure 2-10.

For all tests pre and post-test masses were measured, and digital images were taken. Uncertainty in the mass measurement is ±5 mg. Environmental scanning electron microscopy (ESEM) was employed as a post-test diagnostic to determine the extent of deposition and material system degradation. To prepare the samples for the ESEM the samples were placed in epoxy to preserve the deposit, cross sectioned, placed in Bakelite, and then polished.

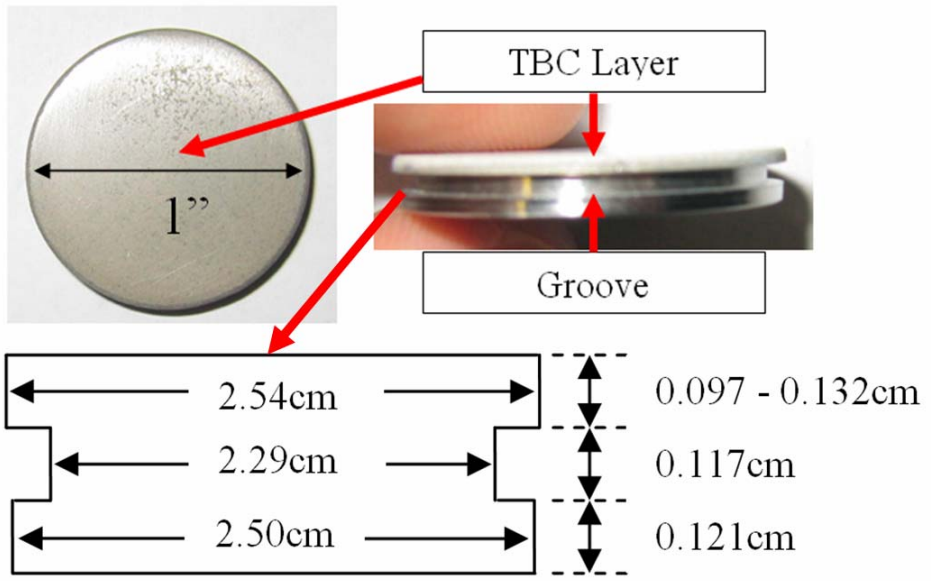

Figure 2-10: Typical pre-test turbine blade button

2.4 Instrumentation

The output from the pressure transducers and K-type thermocouples mounted just upstream of the orifice plates is connected to a National Instruments SCXI chassis.

These pressure and temperature data are monitored by a LabVIEW VI program which allows the operator to maintain the proper mass flow rate of the air. The natural gas flow rate is measured with a rotometer with an attached pressure gauge. This flow rate is adjusted, using the rotometer, to maintain the desired exit temperature while bringing the combustor to steady state and is approximately 5% of the air mass flow rate. The combustor exit temperature is measured by two 0.8 mm diameter Super OMEGACLAD K-type thermocouple probes one of which is mounted just inside the equilibration tube while the other is adjustable. The adjustable thermocouple is positioned in the center of the tube until the combustor is operating at steady state, after which it is removed and the fixed thermocouple is used as the reference during the test. The adjustable thermocouple is periodically inserted into the center of the tube during testing to verify that the exit temperature is maintained at 1183°C. The probes are connected to a National Instruments NI SCXI-1112 thermocouple module mounted in an NI SCXI-1000 chassis. The temperature data at the exit is passed to the same LabVIEW VI program as the air pressures and temperatures data. The LabVIEW VI program calculates the total mass flow rates for the combustor and coolant air. The mass flow rate of the combustor, the data from the thermocouple probes, and the cross-sectional area of the equilibration tube are used to calculate the flow Mach number using the Ideal Gas Law relation for the speed of sound (Eq. 2.6). The specific heat ratio used was that for combustion in air (γ = 1.3) while the gas constant was approximated as being the same as the value for air (i.e. R = 287 J/kgK).

$$M = \frac{\dot{m}}{\rho A \sqrt{\gamma R T}} \tag{2.6}$$

The temperature of the turbine blade surface exposed to the jet at 1183°C (i.e., the frontside temperature) was measured with two different methods. An Ultimax infrared one-color thermometer was used, but the emissivity of the hot coupon surface was unknown. A two-color technique was therefore employed in order to minimize the effect of surface emissivity uncertainty on the calculated temperature. The technique used in the experiment was taken from Lu (2006), and uses the blue and green signals from the RGB ports on a SVS285CLCS Sony Exview HAD CCD camera. The measured spectral response (S_λ) of each color from the RGB camera is shown in Figure 2-11 as a function of wavelength (λ).

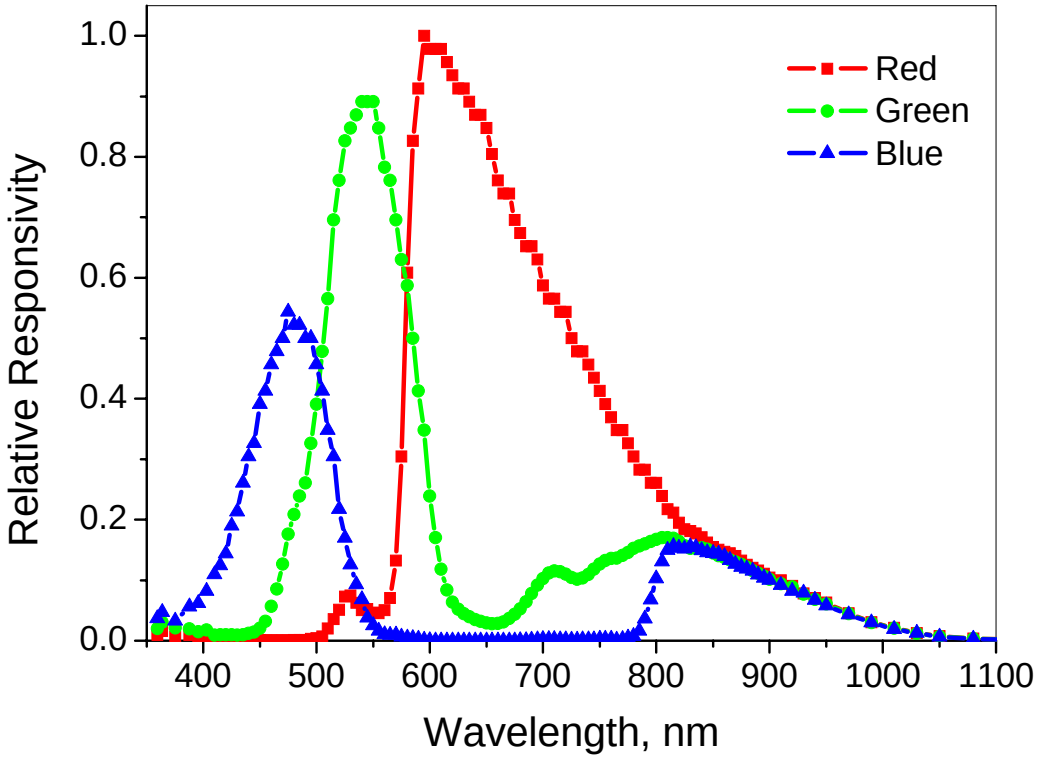

Figure 2-11: Measured spectral response of the SVS285CLCS camera

As explained by Lu (2006), the intensity of radiation measured by the camera's CCD detector (DN) is defined by Eq. 2.7 where ε_λ is the surface emissivity, C_1 and C_2 are the two Planck's law constants, and C_{exp} is a constant that depends on the experimental geometry, exposure time, and gain factor. The value of C_{exp} was calibrated for each color using a blackbody source at temperatures from 530°C to 1130°C.

$$DN = C_{\exp} \cdot \int_{\lambda_1}^{\lambda_2} \varepsilon_\lambda S_\lambda \cdot \frac{C_1 \cdot \lambda^{-5}}{e^{C_2/\lambda \cdot T} - 1} d\lambda \tag{2.7}$$

The temperature of the surface can then be measured using the ratio of detector signals from two colors, as shown in Eq. 2.8.

$$\frac{DN_{Blue}}{DN_{Green}} = \frac{C_{Blue} \int_{\lambda_1}^{\lambda_2} S_{\lambda,Blue} \cdot \frac{C_1 \cdot \lambda^{-5}}{e^{C_2/\lambda \cdot T} - 1} d\lambda}{C_{Green} \int_{\lambda_1}^{\lambda_2} S_{\lambda,Green} \cdot \frac{C_1 \cdot \lambda^{-5}}{e^{C_2/\lambda \cdot T} - 1} d\lambda} \tag{2.8}$$

This technique is very similar to other two-color pyrometry experiments, except that broadband wavelengths are used instead of narrow wavelengths. Lu studied the sensitivity of the different color combinations as a function of temperature and recommended the blue-green combination for the intermediate temperatures studied here. The red-blue combination would be better for higher temperature (~ 1700°C)

applications. Over the range of 950-1150°C, the uncertainty in temperature was estimated at 15.4°C.

A set of experiments was performed to determine the difference between the frontside and backside temperature of the button as a function of the flow rate of backside cooling air. Frontside temperatures were measured for the standard experimental conditions in the TADF (i.e., 1183°C, Mach 0.25) as a function of the backside cooling air flow rate. No particles were injected into the combustor while these data were obtained. Backside temperatures were measured using thermocouples welded to the back surface of the button. The experiment was performed in the morning, followed by a period where the reactor cooled down, and then repeated in the afternoon. The camera and thermometer were not moved in between these experiments to reduce errors due to focal length and location of the focal spot on the button. The frontside temperatures were determined from the image of a rectangular area in the center of the button in order to avoid edge reflections and hot spots. The measured temperature data are shown in Figure 2-12. Both the frontside temperature and the backside temperature decrease with increased cooling. The temperature difference between the frontside and the backside increases as the cooling flow rate increases, as expected, with temperature differences ranging from 200°C to 400°C. There is a discrepancy in the a.m. and p.m. frontside temperature measurements using the BG method at the higher coolant flow rates.

The IR thermometer results are plotted in Figure 2-12 as well. A surface emissivity of 0.2 was used to match the 2-color temperature at the lowest cooling rate. The IR temperature measurements follow the average of the two 2-color measurements at the higher cooling rates with this constant emissivity value.

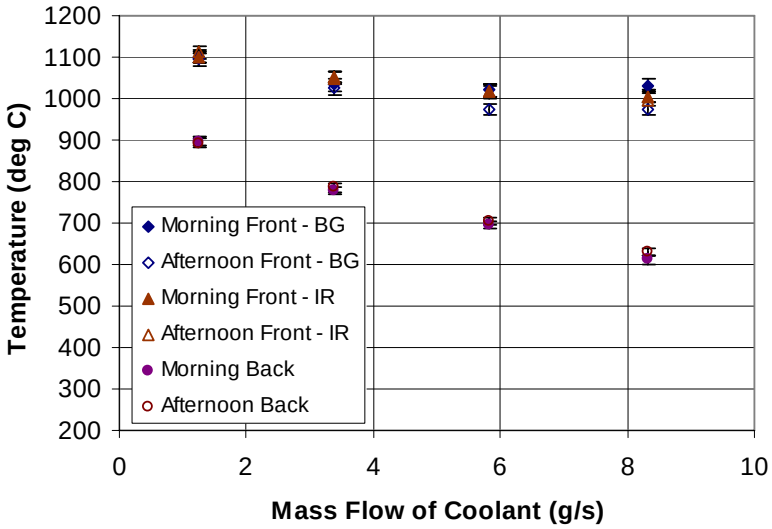

Figure 2-12: Measured frontside and backside temperatures as a function of cooling

The temperatures of the inlet and outlet air streams used to cool the backside of the button were measured with thermocouples for each cooling flow rate. Since the heat capacity of air is known, the heat removed by the cooling stream can be calculated as follows:

$$Q = \dot{m} C_p \left(T_{out} - T_{in} \right) \tag{2.9}$$

The heat removed was divided by the area exposed on the backside of the button in order to obtain an area-averaged heat flux. In addition, the conductive flux through the button under each condition was computed from the average frontside and backside temperatures (Figure 2-12) using estimates for the thermal conductivities of the button

substrate and the thermal barrier coating which were 20 and 1.4 W/mK respectively. The comparison of the computed fluxes is shown in Figure 2-13.

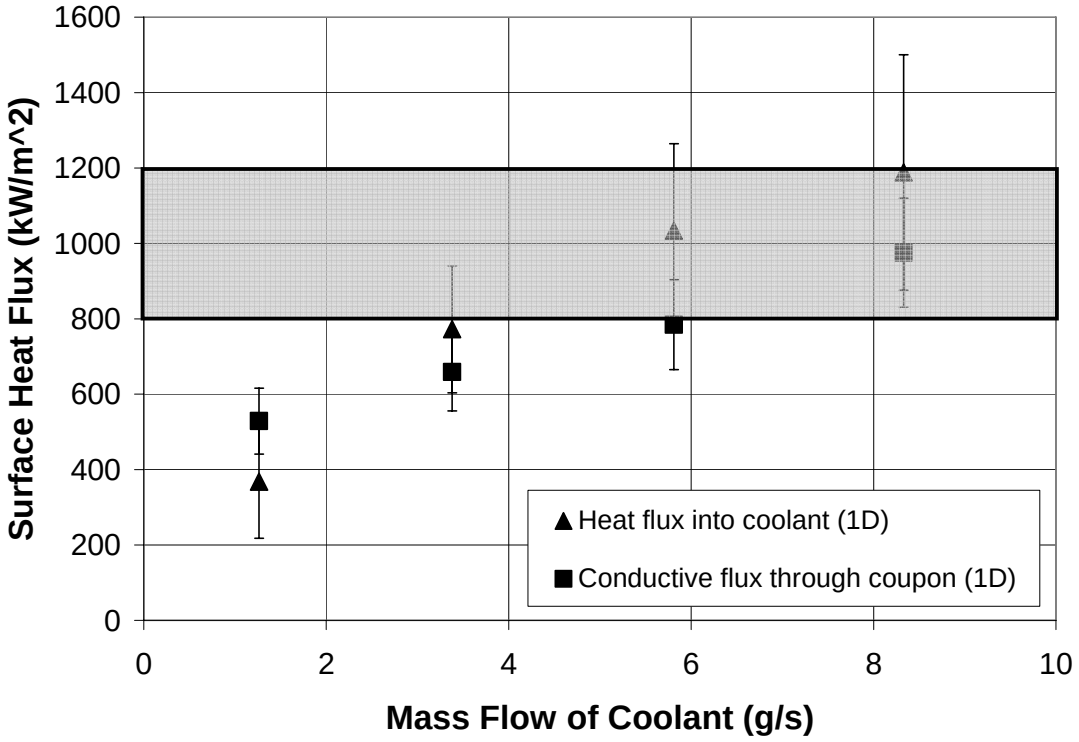

Figure 2-13: Calculated heat fluxes due to conduction through the coupon and due to backside cooling for a coupon in the TADF at 1183°C at Mach 0.25 (The gray band represents heat flux estimates for 1st stage vanes in a modern gas turbine)

The agreement is reasonable considering the simple 1-D analysis employed in the computation. Both heat flux estimates increase with increased cooling, matching the expected trend. Also, the absolute magnitude of heat flux is comparable to estimates for 1st stage vanes in a modern gas turbine (800-1200 kW/m^2, denoted by the gray band in Figure 2-13). The conductive flux is generally lower than the backside cooling flux estimate. This result is consistent with insufficient insulation surrounding the cooling

apparatus to prevent three-dimensional heat flows around the button. Such peripheral heat flows would not register with the backside thermocouple measurement but would eventually make their way into the coolant flow. At the lowest coolant flow rate, the single thermocouple measurement in the coolant exit flow may not be registering a representative "mixed-out" temperature. A more sophisticated analysis is needed to more accurately measure the surface heat flux for future studies.

2.5 Particulate Preparation

To avoid the considerable capital expense and complexity associated with simulating combustor operation with different fuel formulations (e.g. fluidized bed, gas cleanup system, etc.), the TADF (as mentioned previously) employs a natural gas combustor seeded with ash particles. Thus, it is critical to insure that the ash particles are of the same size, state, and composition that might be expected to impact on turbine surfaces after reasonable gas cleanup.

The two ash samples used in this study were coal and petcoke which were collected from external sources. Subbituminous coal fly ash was obtained from an operating power plant, while the petcoke ash is boiler slag obtained from a combined cycle gas turbine power plant operating with a blend of 55% petcoke and 45% coal. A mechanical grinder with a collector to trap the particles exhausted out of the air filter was used to obtain the size particles needed for testing.

Since the objective of the study was to simulate ash that could be entrained by the flow leading to the turbine, the particles must be small enough to navigate the various gas cleanup systems. Filtration systems in modern gas turbine power plants are designed to

remove all particles with diameters greater than 10 μm and a majority of particles larger than 1 μm. Measurements of particle size distributions from properly functioning advanced filtration systems indicate mass mean diameters (MMD) of order 1 μm, even for hot gas clean-up. With inadequate or degraded filtration, these levels can be exceeded. Thus the target mass mean particle diameter for this study was less than 10 μm. This study focuses only on contamination from the fuel gas system. In addition to particles from the fuel stream, sand and dirt from the inlet air and rust from the gas turbine flow path can also form deposits resulting in spallation and TBC loss.

After grinding, the size of each ash sample was determined using a laser-based Coulter Counter. The ash was suspended in distilled water and dispersed through the Coulter Counter feed system with the use of a sonicator and/or small amounts of liquid detergent. When illuminated by the laser beam, the particles scatter light in patterns according to their size. This scattered light was detected using photodetectors and converted to the particle distributions shown in Figure 2-14; mass mean diameters are presented in Table 2-1. Uncertainties in the coal MMD are 15%, 9%, 22%, and 17% for the small, medium, large, and unground sizes, respectively. Uncertainty in the petcoke MMD is 17%. The large uncertainties are mainly due to repeatability as the MMD is an average of several measurements (see Appendix A). The mechanical grinder used was a wheat grinder and the different size particles were taken from various parts of the grinder. The smallest size coal particles and the petcoke particles were collected from the air filter. The medium size coal particles were taken from the collector inside the wheat grinder. The large coal particles were taken from the bucket of the wheat grinder. The bulk density of each ash sample was measured in a graduated cylinder, and the apparent

density (mass per particle exterior volume) was calculated using an estimated packing factor of 0.5.

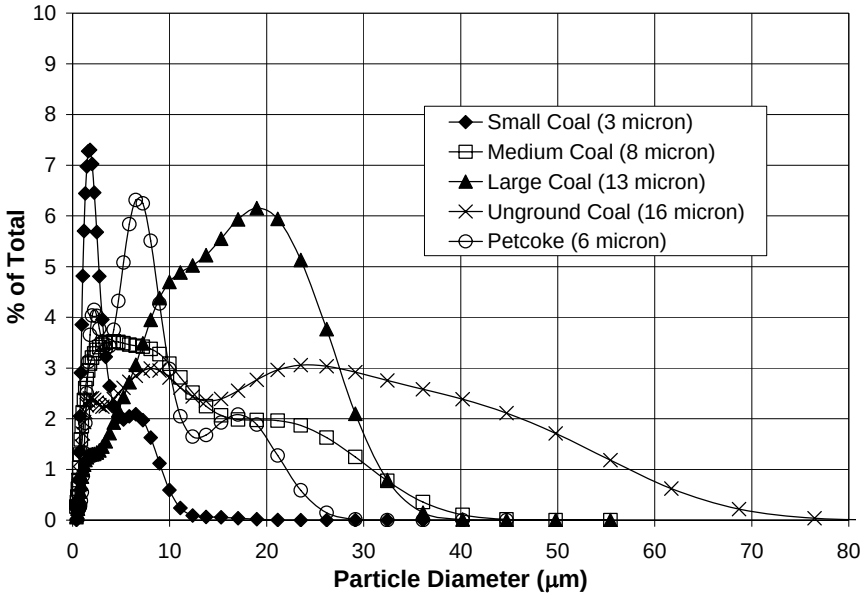

Figure 2-14: Particle size distributions for coal and petcoke ash

Table 2-1: Ash particle summary statistics: size, density, and average elemental composition

	Coal	Petcoke
Mass mean diameter	3.1-16	6.3
Bulk density (g/cc)	0.99	1.45
Apparent density (g/cc)	1.98	2.90
Element	Weight %	Weight %
Na	6.9	4.3
Mg	3.6	2.2
Al	17.8	14.5
Si	47.4	38.3
P	1.6	0.0
S	1.8	1.0
K	2.6	2.5
Ca	8.7	7.5
Ti	1.6	0.8
V	0.0	3.4
Fe	6.4	22.9
Ni	0.0	0.9

Since larger particles (>1 μm) are deposited by inertial impaction while smaller particles (<1 μm) are generally deposited by turbulent diffusion and thermophoresis, the results of this study are appropriate for deposition dominated by inertial impaction. With the exception of some of the unground coal, all of the particles are less than 40 μm in diameter, which Jensen (2004) determined to be the maximum diameter that would attain full velocity and thermal equilibrium with the hot gases in the combustor exit tube of the TADF (see Chapter 2.1). Thus, the particles used for the tests in this work are expected to be at the proper gas temperature before impact.

Following the Coulter Counter measurement, ash samples were placed inside a FEIXL30 environmental scanning electron microscope (ESEM) to obtain qualitative validation of the particle size and shape. Figure 2-15 shows typical ESEM images from the smallest and largest of the coal ash samples.

X-ray spectroscopy was used to determine the composition of the two types of ash while they were in the ESEM. An EDAX Phoenix Spectrometer with super ultra-thin window was used to obtain elements down to an atomic number of carbon. The elemental compositions of the two types of ash, as determined by the x-ray analysis, are given in Table 2-1. Values of 0.0 indicate levels below the background noise level of the spectrometer. An independent elemental analysis was conducted on the two ash samples by ALS Chemex using inductively coupled plasma atomic emission spectroscopy (ICP-AES). The results identified the same elements as the x-ray spectrometer in approximately the same weight percentages, though the ICP-AES analysis of the bulk ash showed 15-20% greater silicon content compared to the x-ray measurements (which were spot measurements). Also, the ICP-AES is unable to measure vanadium. Of particular

note in Table 2-1 is the high level of vanadium found in petcoke (added during petroleum processing). Petcoke also shows particularly high levels of iron-oxide. The corrosive element sodium is present in both of the samples.

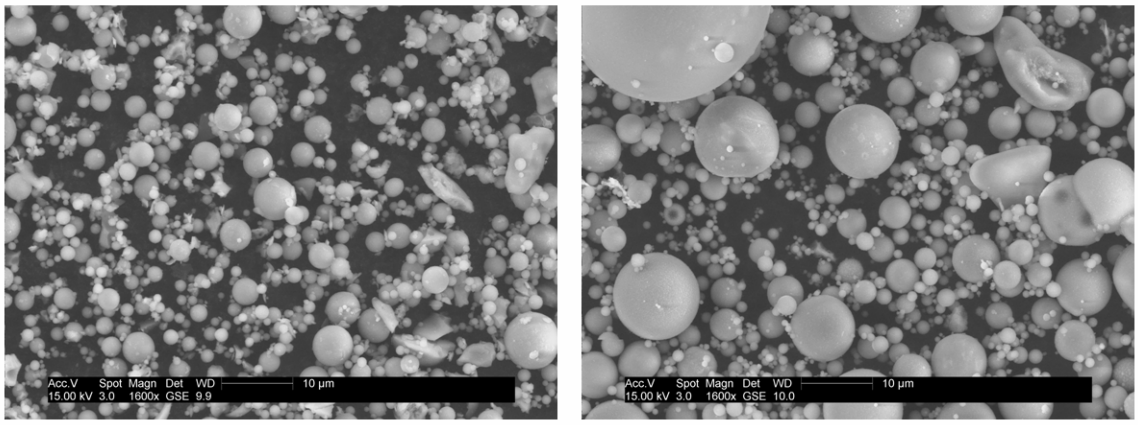

Figure 2-15: ESEM images of smallest (left) and largest (right) size coal particles

3 Particle Size Series Results

3.1 Testing Conditions

Four series of tests were conducted to study the effects of particle size, gas exit temperature, and metal temperature on deposition. The first test series looked at the effects of particle size on deposition. For the case of erosion, Hamed et al. (2004) calculated the trajectories of various sizes of particles (10-50 μm) in a modern LPT stage using a semi-empirical particle rebound model. They found that larger particles actually have multiple rebounds between neighboring blades while smaller particles primarily impact the pressure surface only. To explore the effect of particle size on deposition, the present study used standard combustor operating conditions (gas exit temperature = 1183±5°C, Mach = 0.25) with the first set of 1" diameter turbine blade samples. The tests were run with no cooling air, and the interior passage of the cooling fixture was insulated with blanket insulation material. The backside temperature was measured with two welded K-type thermocouples and found to be approximately 990°C ±10°C, which is roughly 200°C below the combustor exit temperature.

Recently, Wammack et al. (2006) conducted a deposition study using polished TBC turbine samples where the specimens were subjected to four consecutive testing cycles, returning the sample to room temperature between each test. They measured a

significant increase in TBC surface roughness following the first thermal cycling. As a result, this roughened surface was much more susceptible to deposit accumulation compared to the highly polished surface prior to the first test cycle. To account for this effect in the current test series, an initial one hour "burn-in" test was conducted with particulate injection, following which the combustor was shut down. The sample was allowed to cool (for approximately two hours) without removing it from the fixture. Following this, the combustor was again brought to steady state and a standard four hour test was conducted. The four different sizes of subbituminous coal fly ash particulate obtained from different locations in the mechanical grinder were used in this test series. The four particle size distributions (shown in Figure 2-14) are given in weight percent, so in all samples there are a majority of particles (by number) in the range below the mass mean diameter.

Table 3-1 shows the testing conditions for the particle size series. Uncertainty in the net particle loadings was calculated to be between 5.5-7.4 ppmw-hrs. The first test using 3 μm size particles was performed on a button which was not part of the first set of buttons. In fact it was not part of any of the three sets listed in Chapter 2. It came from a set of buttons which proved to not be suitable for testing because the TBC layer had a beveled edge around the circumference of the button. During the first test, spallation occurred across the entire surface of the button, (with the greatest amounts occurring around the entire circumference of the button exposing much of the metal substrate) which seemed suspicious. The test was repeated with a button from the aforementioned first set and very little spallation was observed and only at the leading edge, therefore it was decided to forego further testing with the initial button set.

Table 3-1: Particle size series test conditions using subbituminous coal

Particle Size [μm]	Test Time [hrs]	Operating Temperature [°C]	Net Particulate Mass added to flow [g]	Particle Concentration [ppmw]	Net Particle Loading [ppmw-hrs]
3	5	1183	10.89	26.92	134.62
3	5	1183	10.05	24.85	124.24
8	5	1183	10.35	25.59	127.95
13	5	1183	12.72	31.45	157.25
16	5	1183	13.39	33.11	165.53

3.2 Digital Images

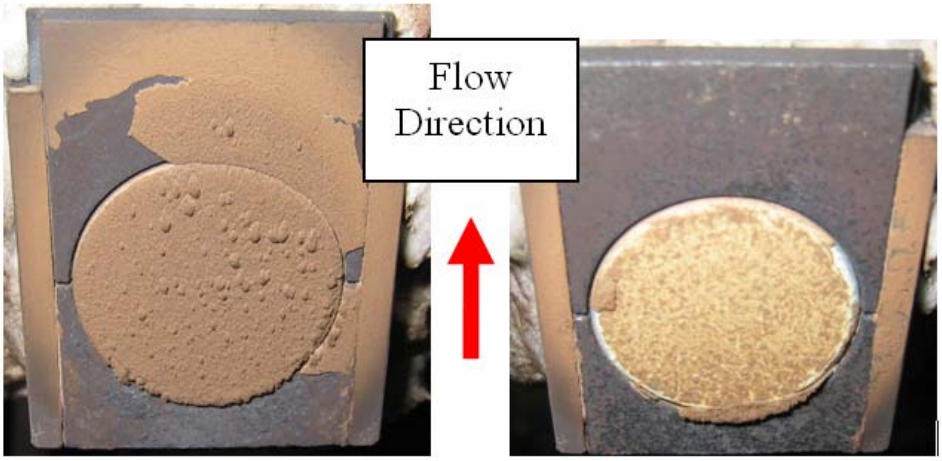

Figure 3-1: Post test images of coupon subjected to 13 μm particle size

Figure 3-1 shows two post-test images of the 13 μm particle test button. The first image was taken immediately after combustor shut-down while the second image was taken after the sample had cooled to room temperature. Streamwise aligned deposit structures are evident in the hot deposit image (Figure 3-1 left). These structures are

similar in appearance to fuel deposit structures previously measured on a serviced turbine blade pressure surface by Bons et al. (2001) (Figure 3-2).

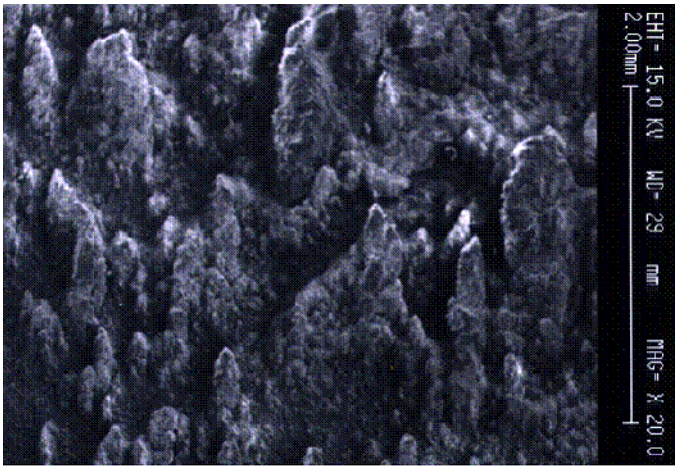

Figure 3-2: Micrograph image taken of deposits found on a turbine blade pressure surface (flow direction is from bottom to top)

The deposits in Figure 3-2 were considerably more tenacious than the accelerated coal deposits in this case, since they were still intact on the blade surface after cool down. With rapid cooling, the mismatch in thermal expansion coefficients between the metal, the TBC, and the deposit results in the removal of most of the deposit with some of the TBC as well. TBC spallation is evident primarily along the leading edge of the circular specimen (Figure 3-1 right), even though the deposit thickness is approximately uniform over the entire coupon (Figure 3-1 left). Wammack et al. (2006) observed similar behavior in their deposition tests and attributed this to the impingement of deposit-laden gas at the exposed metal/TBC interface. Thus, material system degradation (e.g. TBC spallation) was always most significant at the leading edge of the turbine specimen. In a gas turbine, similarly exposed TBC/metal interfaces are evident at each of the film

cooling holes in the stagnation region of the blade. This explains the common occurrence of TBC spallation adjacent to stagnation film holes as described by Bons et al. (2001). The extent of spallation and material system degradation will be discussed further using ESEM images.

Figure 3-3 shows digital images of the post-test buttons immediately after shut down for the particle size series as well as after the buttons cooled to room temperature. Particle size increases from smallest (3 μm) to largest (16 μm) going from left to right. This figure illustrates the substantial deposit separation which occurred while the button cooled to room temperature following combustor shut down. An increase in spallation of the TBC with particle size is also evident from the figure, particularly at the leading edge.

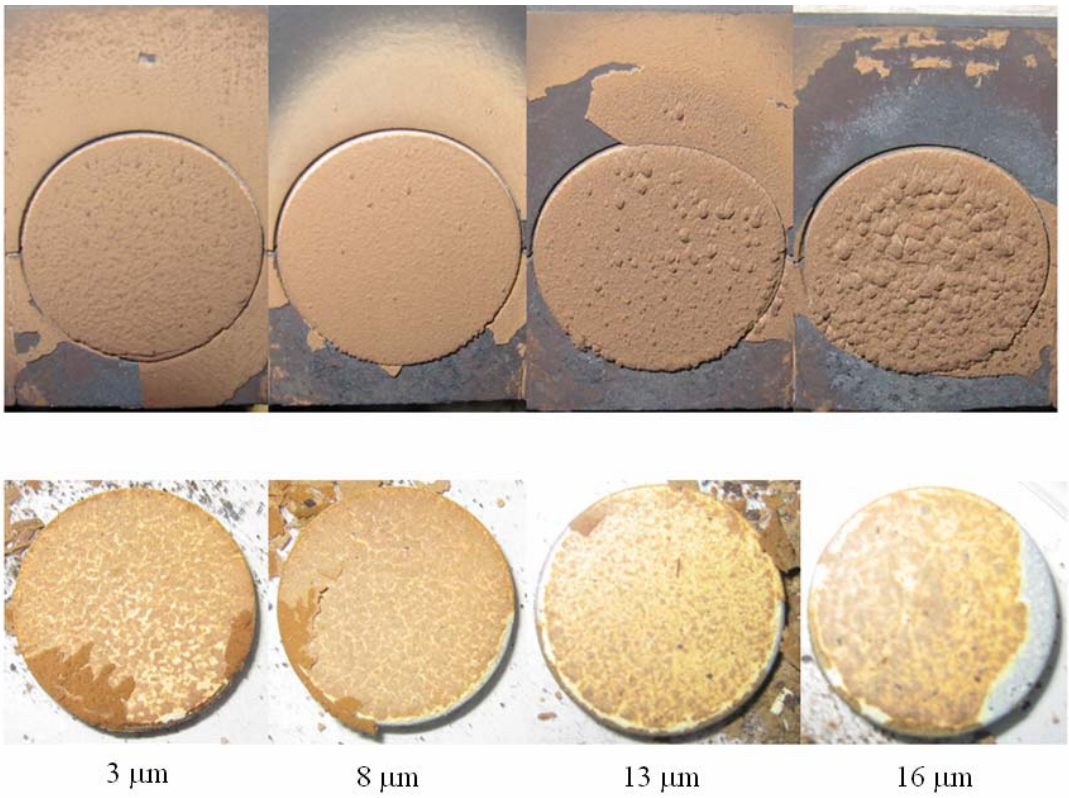

Figure 3-3: Particle size series post-test buttons immediately following shutdown (top) and following cool down to room temperature (bottom)

3.3 Deposition Statistics

Using the pre-test and post-test mass measurements, the net specimen mass gain during exposure was assessed (Table 3-2). In some cases the deposit was very fragile and much of it flaked off following the test as it cooled. The separated deposit percentage, defined as the amount of deposit that separated after the test ended divided by the net specimen mass gain, is also shown in the table. Uncertainty in separated deposit percentage was less than 2%. Percentages greater than 100% are indicative of significant spallation of the TBC layer where the mass of the separated deposit (plus TBC) weighed more than the net specimen mass gain. The increasing percentage of separated deposit with increasing particle size indicates that TBC is more prone to spall with larger deposit formations. The problems associated with the first test using the button with beveled edges is evident in Table 3-2 with the very high separated deposit percentage. However, the repeatability of the TADF is evident in comparing the net deposit mass, deposition rate, and net capture efficiency with that of the repeated test using the set of buttons selected for this test series.

Table 3-2: Deposition results from particle size test series using subbituminous coal

Particle Size [μm]	Preburn Button Mass [g]	Button Mass Change [mg]	Separated Deposit Mass [mg]	Separated Deposit %	Net Deposit Mass [mg]	Deposition Rate [mg/cm^{2}hr]	Net Capture Efficiency [%]
3	14.35	-120	490	132	370	14.60	3.40
3	14.73	70	300	81	370	14.60	3.68
8	14.88	60	450	88	510	20.13	4.93
13	14.12	-10	880	101	870	34.34	6.84
16	14.99	-140	1220	113	1080	42.63	8.07

Dividing the net deposit mass by the exposed button surface area and the test duration yielded deposition rates from 14 ±0.29 mg/cm^{2}hr to 43 ±0.86 mg/cm^{2}hr for the smallest and largest size particles (Table 3-2). Figure 3-4 shows the effect of particle size on net capture efficiency (mg/hr of deposit divided by mg/hr of particulate added to the flow). Capture efficiency increases asymptotically with particle size with a more than 50% increase from 3 μm to 16 μm. Uncertainty in capture efficiency was less than 0.1%. These results suggest that with filter degradation, deposition problems as well as turbine hardware damage are likely to increase considerably. Additionally, it is important to note that even the smallest size particles tested showed significant deposition. This would indicate that even with properly functioning filtration systems the problems associated with deposition and spallation cannot be entirely eliminated.

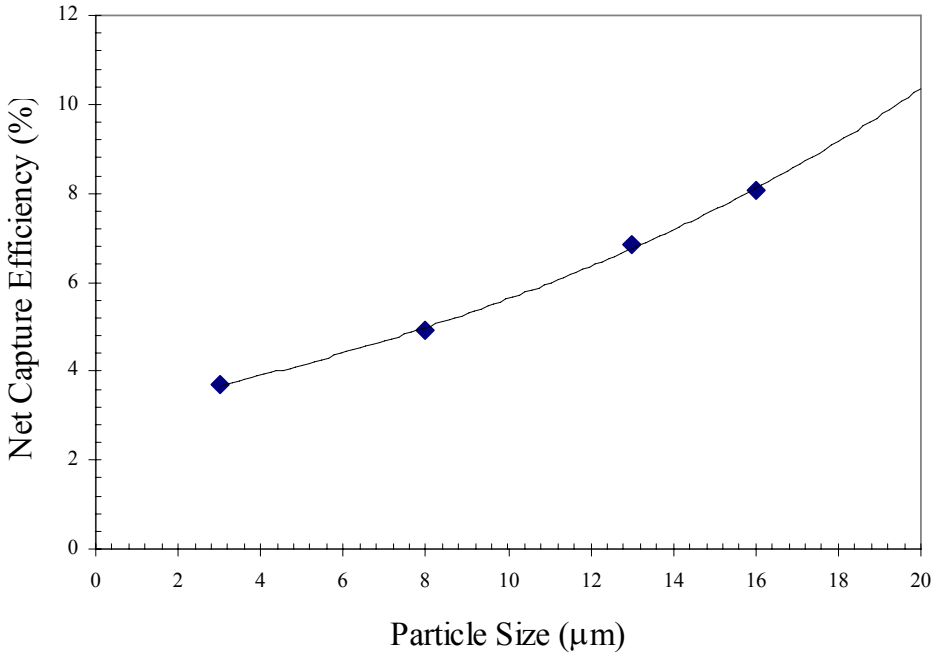

Figure 3-4: Effect of particle size on net capture efficiency

These deposition rates are lower than previous measurements in the same facility (before modifications were made) by Bons et al. (2007) who reported 70-140 mg/cm^{2}hr and those by Wenglarz and Fox (1990) who reported 200-400 mg/cm^{2}hr. The smaller MMD of particles used in this study is one possible reason for the decrease in deposition rate versus Bons et al. Also the new fixture doesn't have any geometric boundaries on the frontside of the button that can trap particles and contribute to deposition like the previous fixture.

3.4 Roughness Measurements

Following testing each button's surface was analyzed with a Hommel Inc. T8000 profilometer equipped with a TKU600 stylus. The Hommel profilometer runs the stylus across the surface of a sample, taking height data at a user-defined number of points during its traverse. Because of the delicate nature of the deposit and the number of traces that would have been required by the profilometer it was not possible to make a 3-D map of the button's surface and take traditional roughness measurements as in previous studies performed using the TADF. The deposit flaking could have potentially damaged the stylus. Also an accurate mapping would have been impossible since the deposit flaking would most likely have caused the stylus to go out of range and abort the measurement. In order to preserve the deposit on the button surface, only a limited number of single traces were performed. Figure 3-5 shows the approximate location at which four 15 mm long traces were taken. The only relevant roughness parameters obtained were Ra, Rt, and Rz. The four traces were averaged and are plotted versus particle size in Figure 3-6 (see Appendix A for uncertainty analysis).

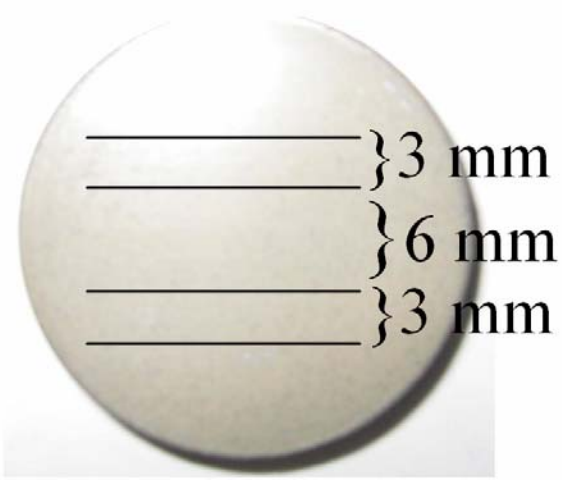

Figure 3-5: Approximate location of the four traces used to calculate roughness values

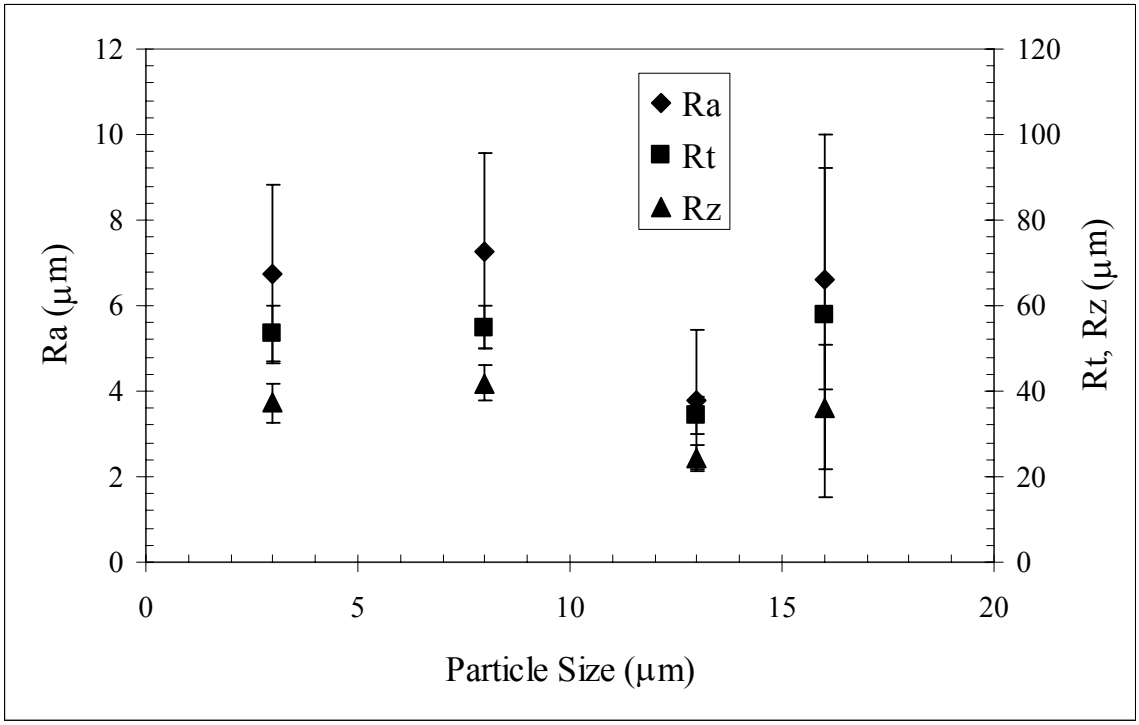

Figure 3-6: Roughness measurements for particle size series

The trend in roughness was somewhat puzzling. An initial increase in Ra, Rt, and Rz from 3 µm to 8 µm was expected as larger particles building up on the surface would

increase the roughness. The 48% drop in Ra (37% in Rt and 41% in Rz) between 8 μm and 13 μm is unexpected. However, after looking at Figure 3-3 one could argue that the large increase in deposit separation does at least appear to make the surface appear smoother after the button has cooled. One possible explanation could be that the larger particles tend to adhere to each other and upon cooling break off leaving a smoother residual deposit layer. However, the roughness values at 16 μm are similar to those at 3 μm which would contradict the proposed explanation. Since the two larger particle sizes are greater than the size normally filtered out, the unexpected trend is perhaps a moot point.

4 Gas Temperature Series

4.1 Testing Conditions

The second test series was performed using coal ash with a mass mean diameter (MMD) of 3 μm with no cooling air and the interior of the coolant passage still insulated. Six tests were performed at five different gas exit temperatures using the second set of samples. Two of the tests were performed at a gas exit temperature of 1183°C which is typical in many modern first stage gas turbine engines while the other tests were at lower temperatures. All of the tests experienced a nominal particulate loading of 96 +/-12 ppmw-hrs. This loading is intended to simulate an engine operating for one year (8,000 hrs) at a low particulate concentration of approximately 0.01 ppmw. Combustor airflow was adjusted to maintain an exit velocity of 170 ±7 m/s for each test, which at the various gas temperatures tested yielded Mach numbers ranging from 0.23-0.26 ±0.03. Since the mode of deposition for particles on the order of 3 μm is inertial impaction, this constant jet velocity condition maintains the same kinetic energy at particle impact. Accordingly, the only relevant variable in this test series is the particle temperature, which was calculated to be in thermal equilibrium with the gas at the exit of the 1 m long equilibration tube. Once the facility reached steady state, particle seeding commenced and lasted for four hours after which the facility was immediately shut down. The initial

one hour "burn-in" test was not performed for this test series. A complete listing of each of the test conditions is shown in Table 4-1. Uncertainty in the net particle loadings was calculated to be between 3.3-5.2 ppmw-hrs.

Table 4-1: Gas temperature series test conditions using subbituminous coal

Particle Size [μm]	Test Time [hrs]	Operating Temperature [°C]	Net Particulate Mass added to flow [g]	Particle Concentration [ppmw]	Net Particle Loading [ppmw-hrs]
3	4	1183	7.88	26.06	104.23
3	4	1183	8.22	27.18	108.73
3	4	1074	7.59	23.35	93.39
3	4	1020	7.82	23.92	95.69
3	4	966	7.36	21.66	86.63
3	4	860	7.86	21.24	84.95

4.2 Digital Images

Digital images of the gas temperature series tests are shown in Figure 4-1. Gas temperature decreases from left (1183°C) to right (860°C). On the top are the buttons immediately after combustor shutdown and on the bottom are the buttons after they cooled to room temperature and were removed from the fixture. Deposits were very similar to the 3 μm test from the particle size series. The same flaking was observed for the tests run at 1183°C, but very little flaking was noticed at lower temperatures. No visual evidence of spallation of the TBC layer was observed at any of the temperatures tested. Note the large amount of separated deposit for the high temperature case (Figure

4-1 far left) and the lack of substantial deposits at low temperature (Figure 4-1 far right) (though the coupon is still discolored at the lower edge near jet impact).

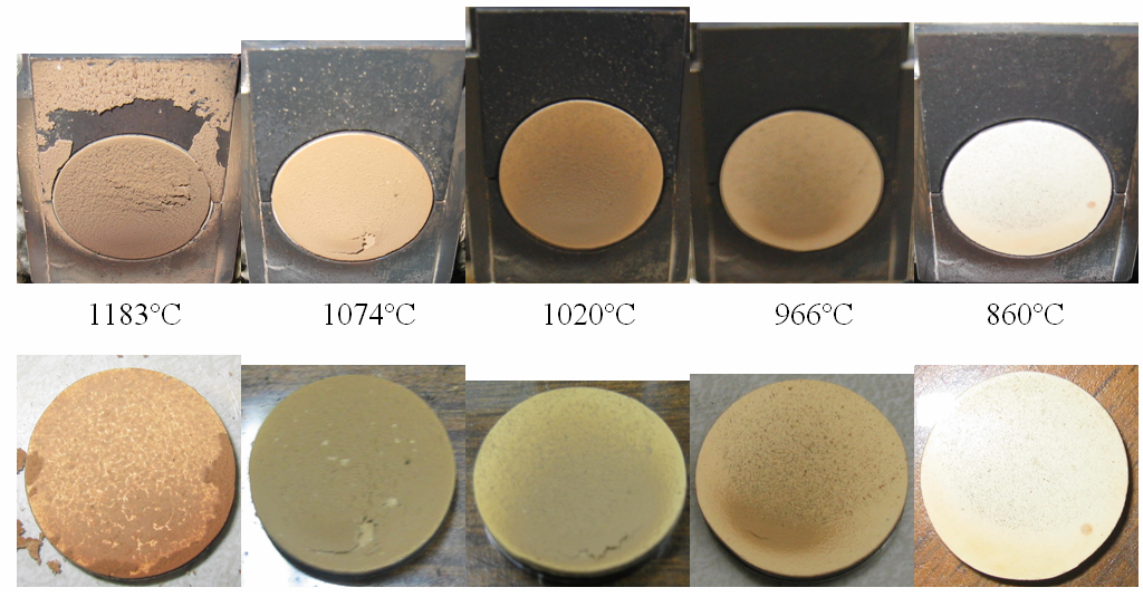

Figure 4-1: Gas temperature series post-test buttons immediately following shutdown (top) and after cool down to room temperature (bottom)

4.3 Deposition Statistics

Deposition results are summarized in Table 4-2. Uncertainty in deposition rate was less than 2.25% for all tests. Repeated tests were run at an exit temperature of 1183°C to show the repeatability of the facility. The deposition rate decreased by approximately 58% with the first 100°C drop in gas temperature. This was followed by another 50% decrease with an additional 50°C drop. An additional 50°C drop in gas temperature to 966°C resulted in a 67% decrease in deposition rate. At 860°C no deposit formed indicating a gas temperature threshold for deposition around 960°C for this study.

This compares well with studies performed previously by Wenglarz and Fox (1990) using coal-derived fuel, who found very small amounts of deposition at a gas temperature of 980°C. Kim et al. (1993) using volcanic ash from Mt St Helens found a threshold temperature of 1120°C. Using a mixture of sand, clay, black scoria, and a claylike additive, Kim et al. found a threshold deposition temperature between 1065-1120°C. Finally Jensen et al. (2005) found a threshold temperature of 900°C using airborne dust composed primarily of Si, Al, Ca, and Mg. Since these gas temperatures are all lower than the melting temperature of the ash compounds, the rising deposition rate with gas temperature is likely due to the increased tendency for deposit sintering at elevated temperatures. Sintering creates large deposit masses that are less susceptible to removal by erosion from subsequent particle impacts.

Table 4-2: Deposition results from gas temperature test series using subbituminous coal

Operating Temperature [°C]	Preburn Button Mass [g]	Button Mass Change [mg]	Separated Deposit Mass [mg]	Separated Deposit %	Net Deposit Mass [mg]	Deposition Rate [mg/cm^{2}hr]	Net Capture Efficiency [%]
1183	13.66	40	100	71	140	6.91	1.78
1183	13.66	40	110	73	150	7.4	1.82
1074	13.64	60	0	0	60	2.96	0.79
1020	13.64	30	0	0	30	1.48	0.38
966	13.69	10	0	0	10	0.49	0.14
860	13.62	0	0	0	0	0	0

The threshold temperature appears to be dependent on a number of factors, most notably the type of particulate. Tests performed by Bons et al. (2007) showed significantly different deposition rates for four different ash particulate types tested at an operating temperature of 1150°C (straw, sawdust, subbituminous coal, and petcoke). A

recent test conducted at an operating temperature of 1183°C using eastern coal particulate showed no significant deposition. The eastern coal contains more Si and Al than the subbituminous coal. The eastern coal also contains much less Ca, Mg, and Na than the subbituminous coal. This suggests that at 1183°C Ca, Mg, and Na tend to deposit to a much greater extent than Si and Al.

Figure 4-2 shows the corresponding decrease in net capture efficiency with gas temperature. Uncertainty in net capture efficiency was less than 1% for all tests. It is noted that the capture efficiency at 1183°C in Figure 4-2 is approximately 50% of that shown in Figure 3-4 for the same 3 μm particle size. This is due to the effect of the one hour "burn-in", which was not performed for this test series. Based on the trend in Figure 4-2 we would expect deposition rates to increase for G and H-class engines which operate above 1500°C. However, some of the constituents may be in the vapor phase at these temperatures, so the degree to which deposition would increase might not be exponential as indicated in Figure 4-2. The author is unaware of any deposition tests in the open literature that operate at higher temperatures than those in this study.

The strong dependency of deposition rate on gas (and particle) temperature has important implications for modern turbine blade rows where the gas temperature can drop by 150-250ºC per stage. If the turbine inlet temperature is high enough so that particles are molten or sinter readily, they may collect primarily near the leading edge – since with falling temperatures through the vane passage, sintering may no longer be possible. If however, the gas temperature at the vane inlet is so high that corrosive elements are in the vapor phase, then they may not deposit on the vane. Rather, they may wait until the temperature drops and then begin to condense on the surface – perhaps in the subsequent

blade row. Another factor affecting deposit buildup is of course the flow angle relative to the local surface. The flow is directly impinging at the leading edge, whereas it is mostly parallel to the wall at mid-span.

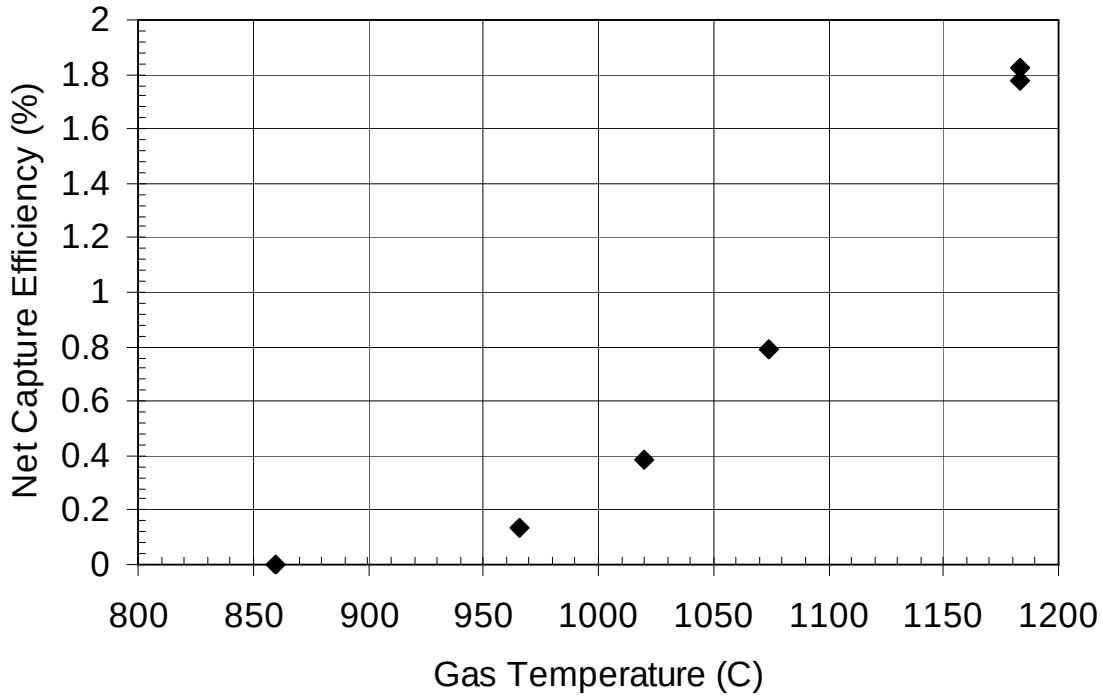

Figure 4-2: Effect of gas temperature on net capture efficiency using subbituminous coal

4.4 Roughness Measurements

Roughness measurements were again taken using the profilometer for the gas temperature series. The same procedure described in Chapter 3.4 was used for this test series as well. The average Ra, Rt, and Rz value for each of the buttons is plotted versus temperature in Figure 4-3. The trend in roughness almost follows that of the net capture efficiency (Figure 4-2). Lower operating temperatures help reduce roughness. The one

exception is for the highest operating temperature of 1183°C. The substantial deposit flaking that occurred with the 1183°C test explains the much lower roughness values compared to the 1074°C test. To account for the deposit flaking, a 3 mm by 1 mm area of a flake taken from one of the 1183°C tests was measured using the profilometer and is included in Figure 4-3. This measurement confirms the trend of decreased roughness with decreasing gas temperature.

Ra decreased by approximately 45% with a 50°C drop in temperature from 1074°C. Another 50°C drop resulted in a drop of approximately 72% in Ra suggesting a threshold temperature around 1000°C where a significant reduction in roughness occurs. The test that experienced no deposition also had virtually no change in roughness.

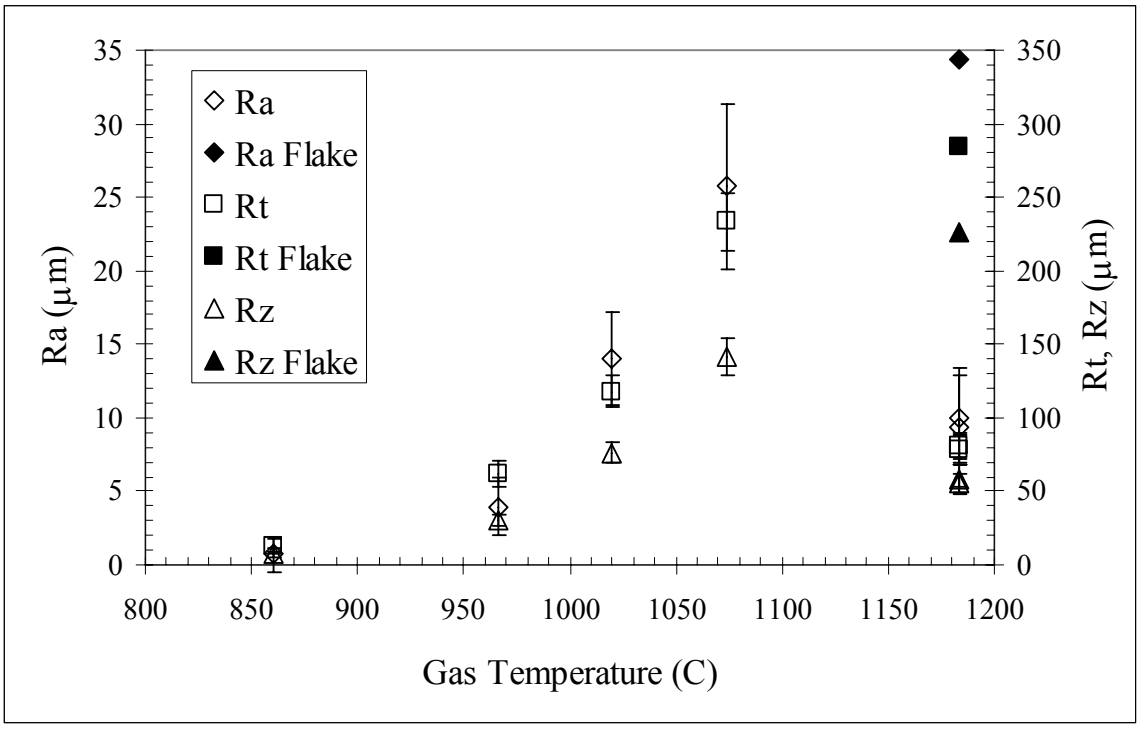

Figure 4-3: Roughness measurements for gas temperature series

At the highest operating temperature the Ra value of the residual deposit layer is approximately 28% higher than the test using the same size particles and operating temperature from the particle size series (Figure 3-6) however, since there was no pre-burn for this test series and the buttons are from different manufacturers a direct comparison is unwise. The fact that the repeat tests at 1183°C had very similar Ra, Rt, and Rz values is interesting to note. Both samples had very similar deposit separation and the residual deposit left on the buttons was similar as well.

5 Impingement Cooling Series Coal

5.1 Testing Conditions

The third test series was performed to study the effects of impingement cooling on deposition. The insulation was removed from the interior of the cooling fixture and two K-type thermocouples were welded to the backside of each sample to measure the backside temperature. This test series used the same set of buttons as in the particle size series. The RGB camera was used to measure the sample frontside temperature and two K-type thermocouples were used to measure the incoming and outgoing coolant temperature. Four tests were run at varying mass flows of coolant. The same coal ash was used as in the gas temperature series (3 μm diameter) and the standard combustor operating conditions, as used in the particle size series, were used including the initial one hour "burn-in" test. All of the tests experienced a nominal particulate loading of 110 +/-7 ppmw-hrs, only slightly higher than the gas temperature series due to the additional one hour "burn-in" test. The no cooling test data were taken from the particle size series test that used 3 μm diameter particles. Since the buttons were from the same set, the particle size series test could be used for a direct comparison to the impingement cooling results. The individual testing conditions are summarized in Table 5-1. Uncertainty in the net particle loadings was calculated to be between 4.5-5.6 ppmw-hrs.

Table 5-1: Coal impingement cooling series test conditions

Mass Flow of Coolant [g/s]	Particle Size [μm]	Test Time [hrs]	Operating Temperature [°C]	Net Particulate Mass added to flow [g]	Particle Concentration [ppmw]	Net Particle Loading [ppmw-hrs]
0	3	5	1183	10.05	24.85	124.24
1.26	3	5	1183	8.48	20.97	104.83
3.38	3	5	1183	9.27	22.92	114.60
5.81	3	5	1183	8.12	20.08	100.38
8.33	3	5	1183	9.54	23.59	117.94

5.2 Digital Images

Digital images of this series are shown in Figure 5-1. The no cooling test (taken from the particle size series) is shown on the left. The amount of coolant used increases from left to right in the figure. As evident from Figure 5-1 the deposits formed in this test series were much more tenacious than the previous ones. Appreciable deposit flaking (apart from the no cooling case) was only observed for the 1.26 g/s cooling case and it was minimal. This result is consistent with the behavior of the gas temperature series in which the lower gas temperatures showed a more tenacious deposit. The applied coolant lowers the temperature of the TBC surface producing a thinner deposit layer. Thin deposit layers are not as susceptible to flaking induced by thermal contraction during cool down. Also, if the turbine is slowly decommissioned deposit layers are not as susceptible to flaking. This was found through two tests conducted at standard operating conditions using 3 μm subbituminous coal with no impingement cooling (fixture interior insulated). In the first test the usual shutdown procedure for the TADF was used (immediate

shutdown following completion of the four hour test). In the second test the immediate shutdown of the TADF was replaced with a two hour decommissioning in which the gas temperature was reduced by 50°C every 15 minutes. Following the two hour decommissioning the combustor was shutdown. The second test had a deposit which was much more tenacious than the first test. The difference in deposition rate was less than 7% and the difference in net capture efficiency was less than 2% between the two tests. The separated deposit percentage of the test with the two hour decommissioning was 68% less than the test that had an immediate shutdown.

A minimal amount of spallation of the TBC layer is visually present at the leading edge of the 1.26 g/s cooling case as well as the 5.81 g/s case. Note at the highest coolant level (far right of Figure 5-1) very little deposit can be seen at the leading edge while the remainder of the button is only discolored.

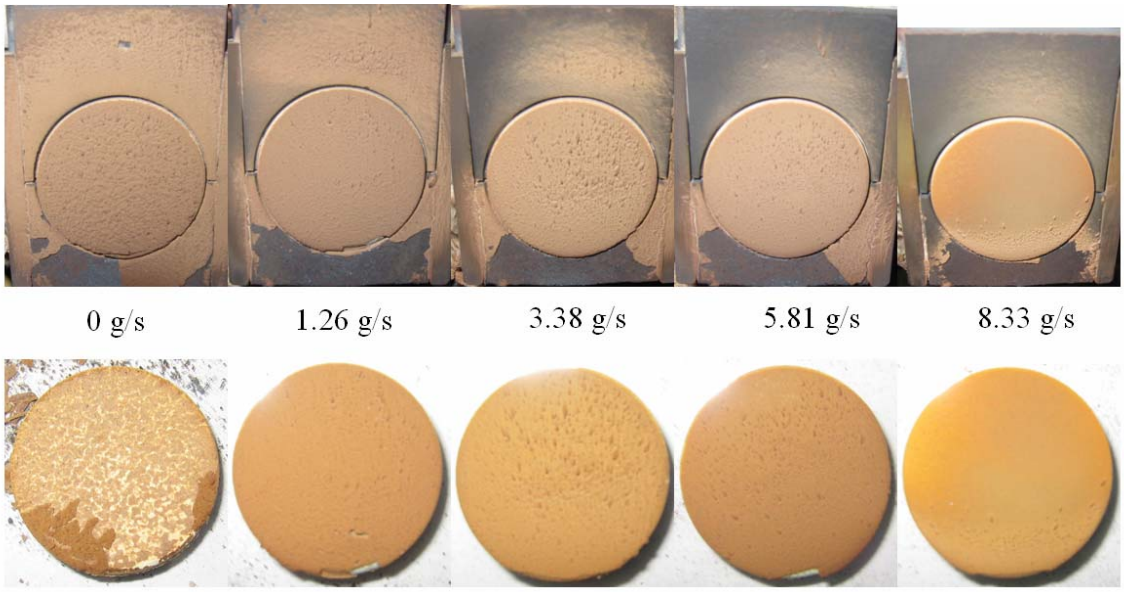

Figure 5-1: Coal impingement cooling series post-test buttons immediately following shutdown (top) and after cool down to room temperature (bottom)

5.3 Deposition Statistics

Table 5-2 provides a summary of the deposition results. Uncertainty in deposition rate was less than 2% for all tests and net capture efficiency uncertainty was less than 0.25% for all tests. The deposition rate was reduced by approximately 40% with the initial level of cooling. This was followed by further reductions as the amount of cooling was increased. Corresponding trends in net capture efficiency are shown in Figure 5-2.

Table 5-2: Deposition results from coal impingement cooling series

Mass Flow of Coolant [g/s]	Heat Flux [kW/m^2]	Preburn Button Mass [g]	Button Mass Change [mg]	Separated Deposit Mass [mg]	Separated Deposit %	Net Deposit Mass [mg]	Deposition Rate [mg/cm^{2}hr]	Net Capture Efficiency [%]
0	0	14.73	70	300	81	370	14.6	3.68
1.26	500.68	30.56	130	90	41	220	8.68	2.59
3.38	1049.21	30.69	120	20	14	140	5.53	1.51
5.81	1404.35	30.53	100	0	0	100	3.95	1.23
8.33	1614.26	30.93	0	0	0	0	0	0

For this series, spallation occurred, but was limited to very small portions of the edge at the base of the sample. The amount of visible spallation decreased slightly with increased coolant mass flow. The drop in capture efficiency noted in Figure 5-2 is similar to the result of Wenglarz and Fox (1990) who observed a factor of 2.5 reduction in deposits for a 200°C drop in metal surface temperature produced by sub-cooling. The present results show a factor of 4 reduction in deposits for a 360°C drop in backside temperature (100°C drop in frontside temperature – see Figure 2-12) with cooling. These results clearly show the benefits of cooling in reducing deposition. However, in G and H class engines the amount of cooling needed to obtain the necessary drop in frontside temperature could be prohibitive. These results also suggest that film cooling could

provide an additional reduction in deposition and spallation. However, Bons et al. (2001) noted that film cooling holes introduce exposed TBC/metal interfaces that are actually more prone to spallation.

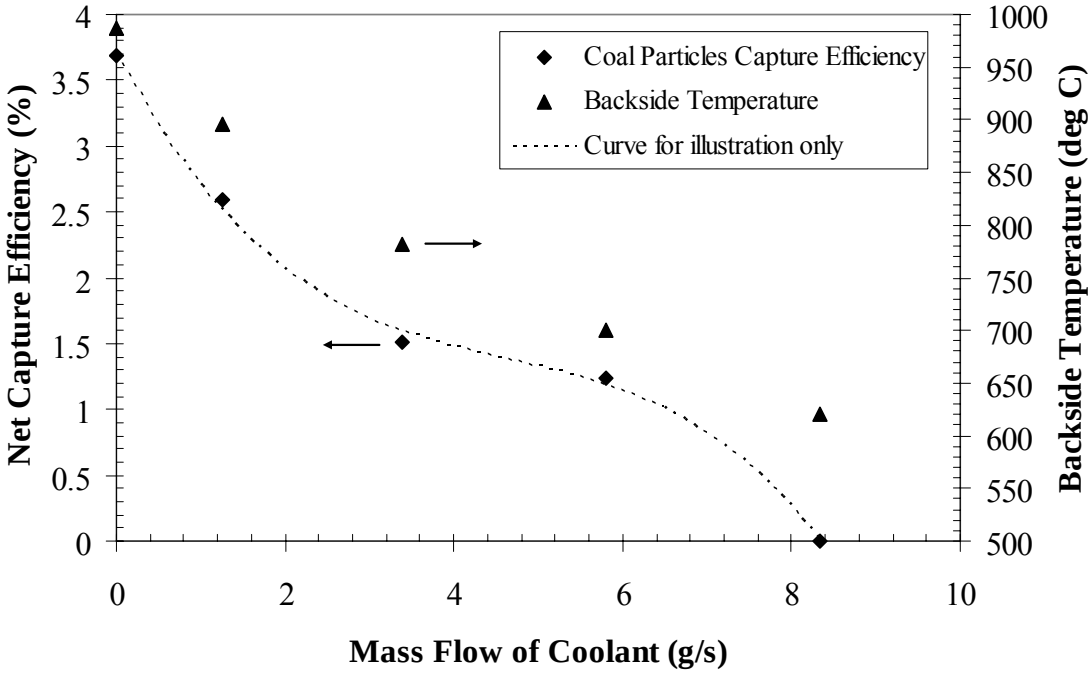

Figure 5-2: Effect of impingement cooling on net capture efficiency

5.4 Roughness Measurements

The profilometer was used to take roughness measurements for this series as well. The same procedure used in the previous two test series was used in this one to take the roughness measurements. The average roughness values for each of the buttons are plotted versus amount of impingement cooling in Figure 5-3. A very interesting trend is seen in this figure. Roughness initially increases with increasing coolant mass flow

followed by a reduction in roughness beyond the 3.38 g/s cooling level. The smallest mass flow of coolant caused a 73% increase in roughness (Ra, Rt, and Rz) over the no cooling case. It also caused a reduction in separated deposit of approximately 50% which could explain the substantial increase in roughness.

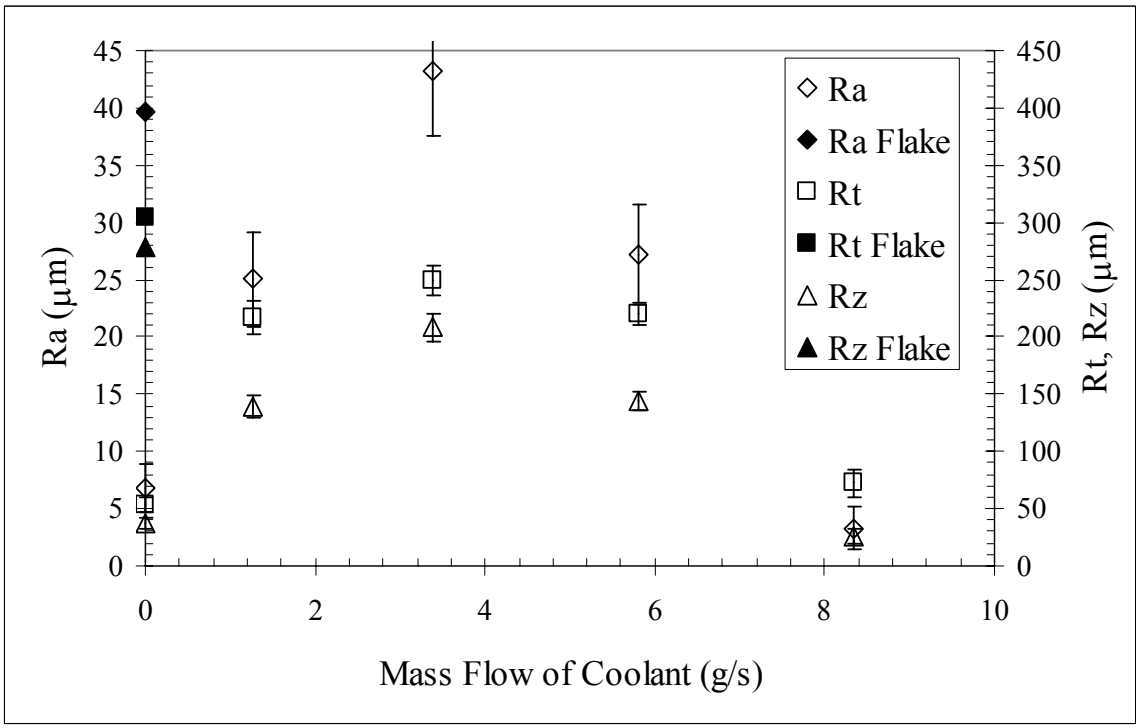

Figure 5-3: Roughness measurements for impingement cooling series using subbituminous coal

A 3 mm by 1.5 mm section of a separated deposit flake taken from the no cooling test was measured using the profilometer. The results are included in Figure 5-3. Rt and Rz are much higher and suggest a trend of decreased roughness with increased coolant. The Ra value doesn't quite exceed that of the 3.38 g/s coolant test; however the flake's location on the button is unknown. The 3.38 g/s coolant mass flow case caused an increase in Ra of approximately 42% from the 1.26 g/s case. It also caused a reduction of

42% in separated deposit and had almost no deposit separation. Unfortunately no flake was available from the 1.26 g/s test to measure its roughness. If the overall trend is decreased roughness with increased coolant this point would be considered an outlier because of the small amount of deposit flaking that could have biased the results.

The 5.81 g/s coolant case reduced Ra from the 3.38 g/s case by almost the same amount as the 3.38 g/s case increased it from the 1.26 g/s case. Since the net deposit mass, deposition rate, and net capture efficiency for these two cooling levels are not that different (Table 5-2) the nature of the deposit must be significantly different to result in such a large reduction in roughness. Additional coolant reduced Ra by 88% but as can be seen from Figure 5-1 this is a result of the reduction in overall deposit as there is only a small amount of deposit at the leading edge of the button and the rest is very smooth. Since the traces were each 15 mm most of the measured surface had almost no deposit present.

After including the deposit flake from the no cooling test, there is some evidence to suggest that increased cooling reduces roughness as the amount of deposition is reduced. However, the 1.26 g/s test is an outlier as there was no flake suitable from which to measure roughness which could have further substantiated the trend.

5.5 ESEM Analysis

To further assess the level of TBC degradation, the test articles from this test series were analyzed using the ESEM. In order to perform this analysis several intermediate steps were taken. The buttons were first placed in epoxy to preserve the deposit. The samples were cross sectioned down the middle using a water-jet cutter. The

cut was made in the direction of the flow over the button. The cross-sectioned samples were then placed in Bakelite to aide in polishing. The samples were polished in steps first using fine grit sandpaper and then using 1 μm diamond paste applied to a felt polishing cloth. Carbon tape was applied to the polished samples to make them conductive for the ESEM.

The cross sectioned samples were first used to measure the thickness of deposit remaining on the surface (Figure 5-4). Uncertainty in the ESEM measurements (of deposit thickness) was estimated at 2% (see Appendix A). Three images were taken of the cross sectioned sample: one at the bottom of the sample (closest to the combustor exit), one near the middle, and one at the top. Figure 5-5 shows a typical series of images taken from the 5.81 g/s cooling level sample. As seen in Figure 5-4, residual deposit thickness is fairly uniform for the no cooling and lowest level of cooling cases. This is indicative of the large percentage of separated deposit for these two cases as noted in Table 5-2. A flake taken from the no cooling case was measured using calipers and its averaged thickness was added to the residual deposit (Figure 5-4). Since the location of the flake on the button was unknown the flake thickness was added to all three locations based on the apparent deposit uniformity (as well as deposit separation uniformity) in Figure 5-1. A flake was also taken from the lowest level of cooling case and the same procedure was performed however the flake thickness was only added to the bottom and middle locations as they were the only regions that showed deposit flaking (Figure 5-1). While this procedure has an unquantifiable amount of uncertainty in terms of the magnitude of deposit thickness, its effect on the overall trend has a high degree of probability, namely decreased deposit thickness with increased cooling.

As the amount of cooling was increased to 3.3 g/s, the top deposit thickness dropped off considerably while the middle and bottom residual thickness continued to increase because of the more tenacious deposit formation near the leading edge. If the deposit flaking is taken into account the middle and bottom total deposit thickness likely decreased at the 3.3 g/s coolant level. Since the top of the button was furthest from the jet it experienced the lower temperatures and thus less deposition. Further increases in the amount of coolant result in decreasing deposit thicknesses at all locations. This spatial variation in deposit thickness is similar to what occurs in an actual turbine with deposition buildup at the hottest spots near the leading edge (Bons et al., 2001).

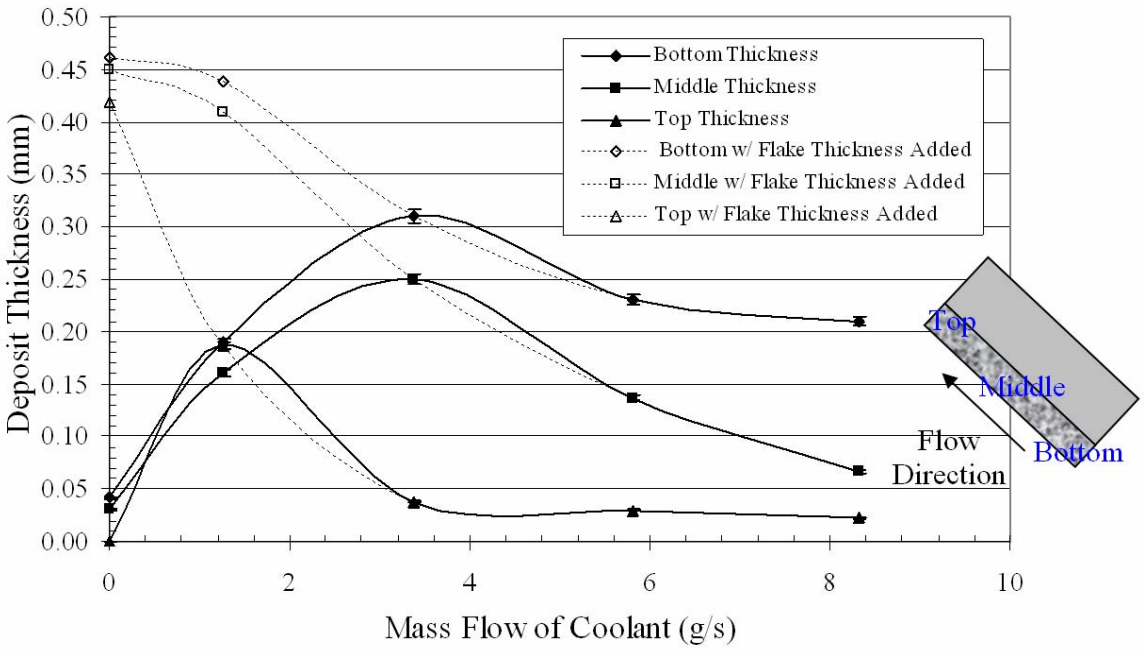

Figure 5-4: Remaining deposit thickness as a function of cooling level

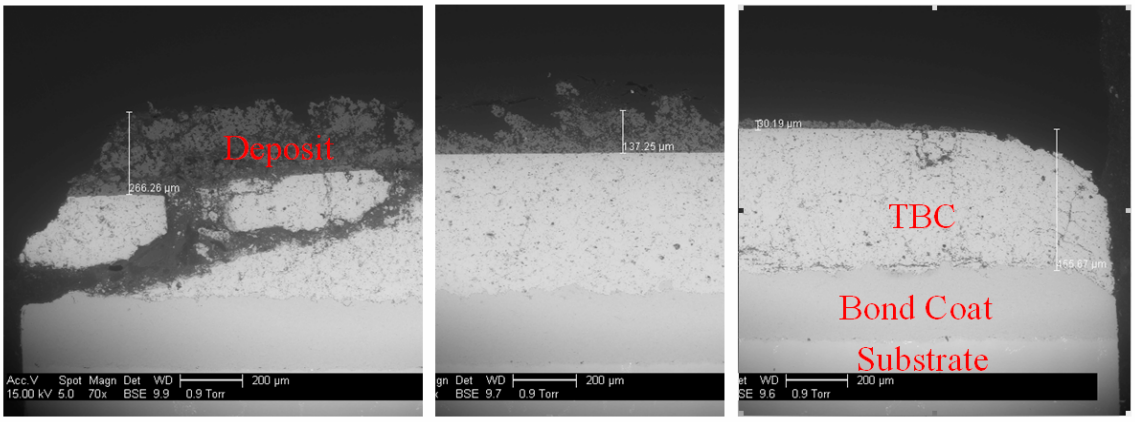

Figure 5-5: Typical image series of bottom (left), middle, and top (right) portions of 5.81 g/s coolant test sample

Figure 5-5 shows the level of spallation which occurred at the leading edge as a result of deposit penetration. Similar spallation was seen in the particle size test series. Wammack et al (2006) observed a similar deposit penetration effect although with a different TBC material system. With the exception of the highest cooling case all other tests in this series had varying amounts of spallation damage caused by penetration of the deposit along the cross section.

X-ray spectroscopy was conducted to determine the elemental constituents in the surface deposit, as well as the penetrating deposits. Uncertainty in the measurements was estimated at 10% (see Appendix A). Figure 5-6 shows the elemental composition in weight percent compared with the ash. The surface deposits showed a similar makeup as the ash, however there was a significant increase in Ca while Na and Si showed large decreases. The figure also clearly shows that the TBC studied is penetrated by Si, Ca, and Al from the ash. The spallation appears to be the result of the difference in coefficients of thermal expansion between the TBC and the penetrating ash elements. Upon shutdown of the facility, this mismatch in contraction rates causes significant

thermal stresses in the TBC, resulting in separation of the TBC layer particularly near the edges of the button.

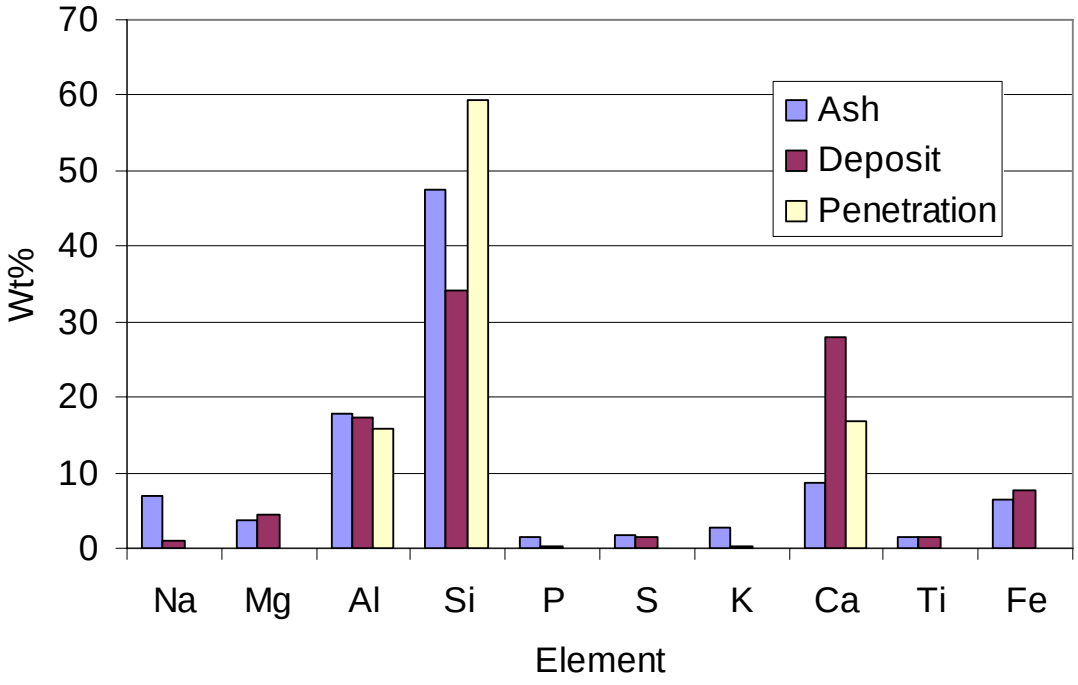

Figure 5-6: Elemental comparison of ash, deposit, and penetration for coal impingement cooling series

6 Impingement Cooling Series Petcoke

6.1 Testing Conditions

A final series of tests were performed using the petcoke/coal blend particulate. Three tests were conducted using particles with a MMD of 6 μm. The third set of buttons described in Chapter 2.3 was used in this test series. First, a no cooling test was performed with the interior of the coolant fixture insulated as in the gas temperature and particle size test series. Following this, two impingement cooling levels were tested in the same configuration as the coal series. The same standard operating conditions were used, namely T = 1183±5°C, Mach = 0.25. The initial one hour "burn-in" was performed for this test series. The testing conditions are summarized in Table 6-1. Uncertainty in the net particle loadings was calculated to be between 4.25-4.53 ppmw-hrs.

Table 6-1: Petcoke impingement cooling series test conditions

Mass Flow of Coolant [g/s]	Particle Size [μm]	Test Time [hrs]	Operating Temperature [°C]	Net Particulate Mass added to flow [g]	Particle Concentration [ppmw]	Net Particle Loading [ppmw-hrs]
0	6	5	1183	7.72	19.09	95.44
3.38	6	5	1183	8.20	20.27	101.37
8.33	6	5	1183	7.68	18.99	94.94

6.2 Digital Images

Digital images of this series are shown in Figure 6-1. The no cooling test is shown on the left. The amount of coolant used increases from left to right in the figure. The deposits looked similar to those of the coal impingement cooling series. The same large amount of flaking occurred on the no cooling case, however there was more flaking on the cooling cases compared to the coal series perhaps due to the larger particle size. There was slightly more spallation of the TBC in the no cooling case compared to the coal, however the different MMD makes a direct comparison difficult.

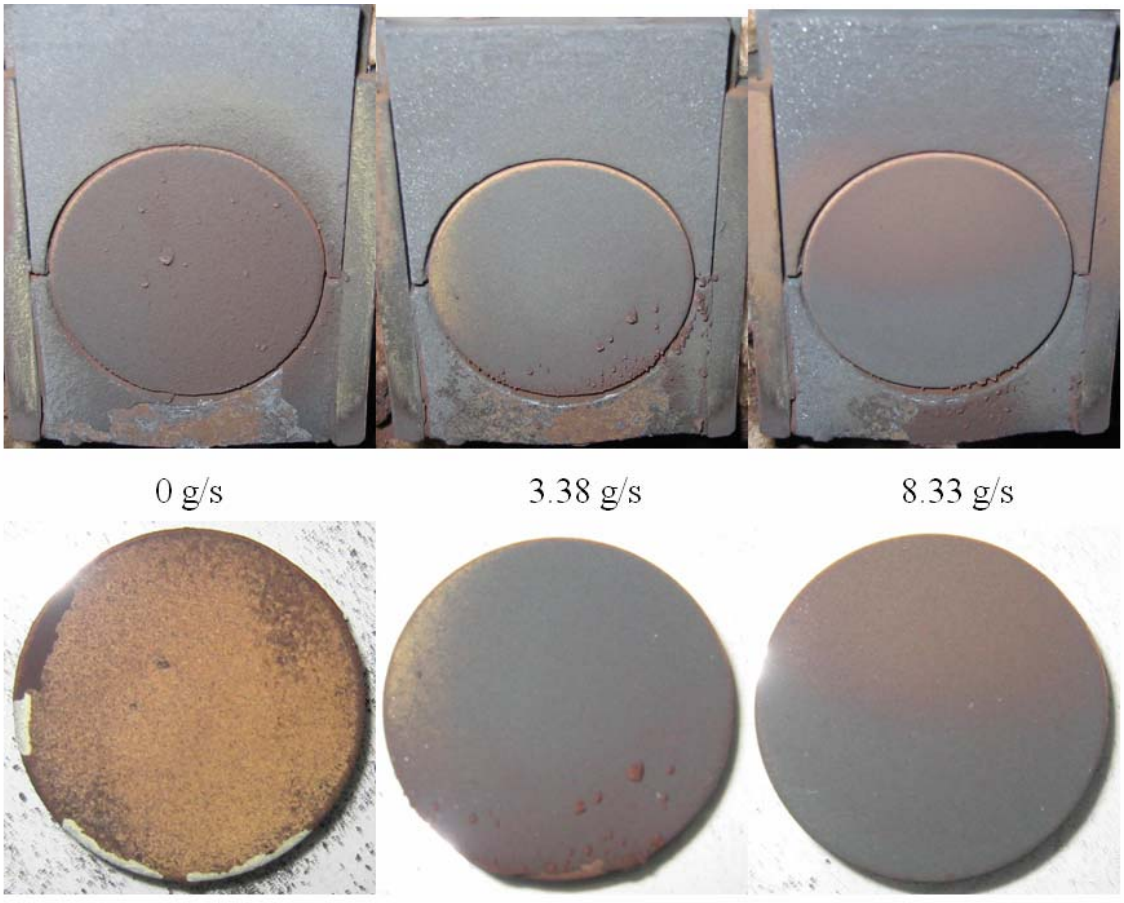

Figure 6-1: Petcoke impingement cooling series post-test buttons immediately following shutdown (top) and after cool down to room temperature (bottom)

6.3 Deposition Statistics

A summary of the deposition results is shown in Table 6-2. Uncertainty in deposition rate was less than 2% for all tests. Trends in net capture efficiency are included in Figure 6-2 with the coal. Uncertainty in net capture efficiency was less than 0.5% for all tests. It is interesting to note that the deposition rate for the no coolant case is the same as that of the coal impingement cooling series (Table 5-2) although the net capture efficiency is 23% higher. The 3.38 g/s coolant test reduced the deposition rate by 73% compared to a 62% reduction for the same amount of coolant in the coal impingement cooling series. The net capture efficiency is also slightly lower for the petcoke than for the coal at the 3.38 g/s coolant flow rate. At the highest coolant mass flow rate a measurable deposit still formed in this series while the coal series had no measurable deposit (although visually there was deposit near the leading edge (Figure 5-1)). Since the petcoke had a slightly larger MMD, and the buttons used for this test series are from a different manufacturer, it is difficult to make a direct comparison, but clearly both fuels show strong similarities in terms of their deposition properties. As was the case with the coal series, cooling clearly helped to reduce deposit formation and protect the TBC layer.

Table 6-2: Deposition results from impingement cooling test series using petcoke

Mass Flow of Coolant [g/s]	Heat Flux [kW/m^2]	Preburn Button Mass [g]	Button Mass Change [mg]	Separated Deposit Mass [mg]	Separated Deposit %	Net Deposit Mass [mg]	Deposition Rate [mg/cm^{2}hr]	Net Capture Efficiency [%]
0	0	13.8	10	360	97	370	14.6	4.79
3.38	1049.21	29.4	40	60	60	100	3.95	1.22
8.33	1614.26	29.42	20	30	60	50	1.97	0.65

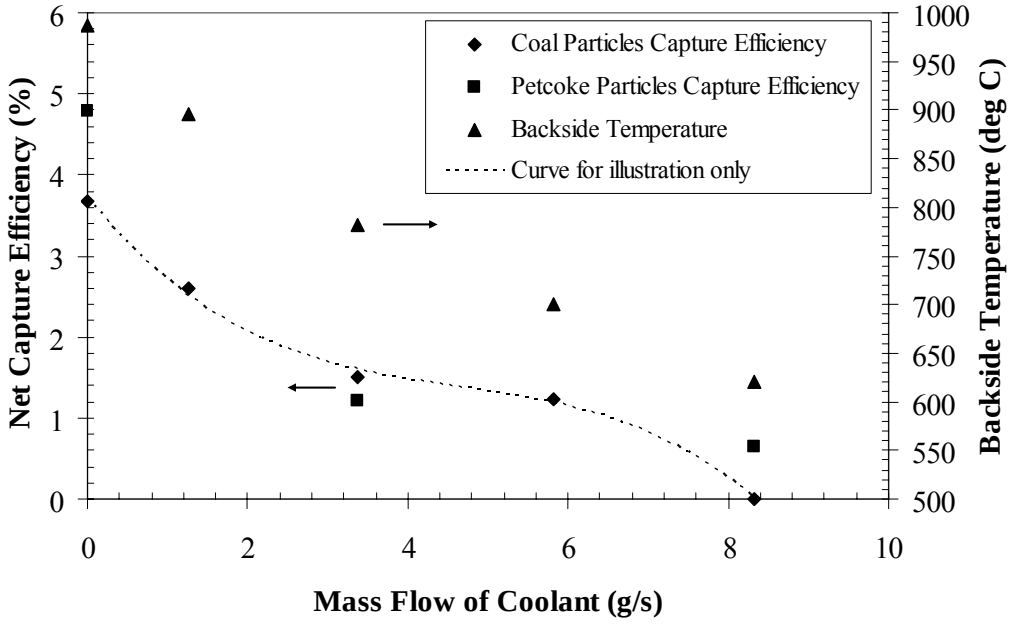

Figure 6-2: Effect of impingement cooling on net capture efficiency

6.4 Roughness Measurements

The profilometer was used to take roughness measurements for this test series however, a slightly different procedure from the one described in Chapter 3.4 was used. Instead of four traces, six were averaged. The traces were spaced 2 mm apart (instead of 3 mm) and the gap in the middle of the button was 4 mm (instead of 6 mm). The averaged roughness values are plotted in Figure 6-3 versus amount of coolant used.

The same trend as seen in the coal impingement series (Figure 5-3) is found in Figure 6-3 as well. The no cooling test was very smooth because of the separated deposit, while the cooling caused an increase of approximately 75% in Ra initially. However, a 3 mm by 1.5 mm section from a flake taken from the no cooling test was measured and is plotted in Figure 6-3. Similar to the impingement cooling series with

coal, the flake revealed a much rougher surface than the residual deposit. The trend of reduced roughness with increased cooling is very apparent from Figure 6-3.

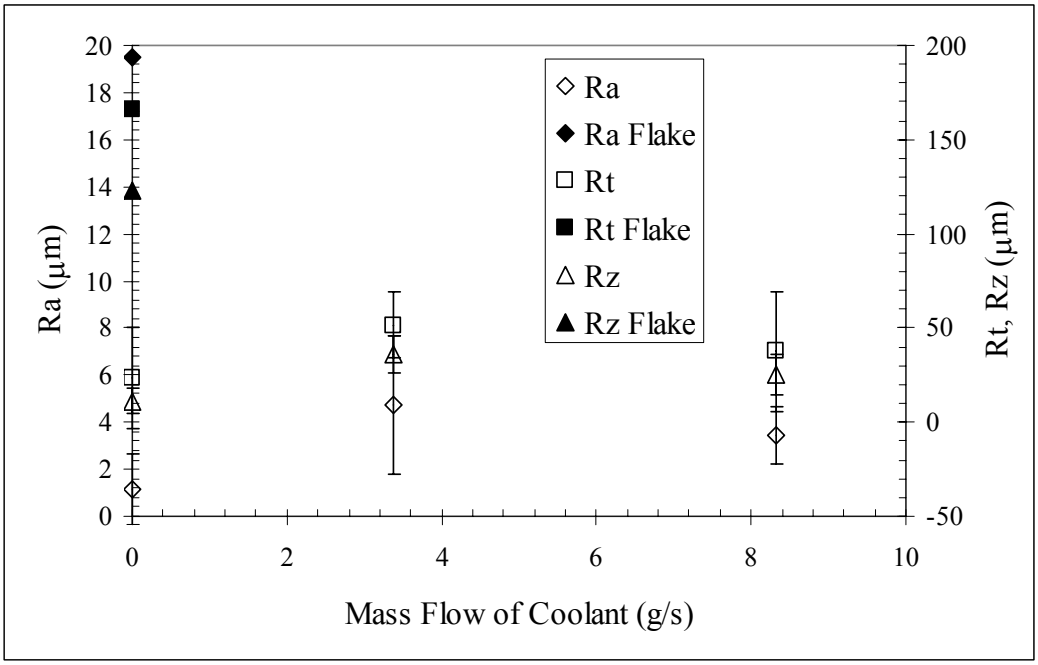

Figure 6-3: Roughness measurements for impingement cooling series using petcoke

The highest coolant level (8.33 g/s) reduced Ra by 27% from the 3.38 g/s test. One glaring difference between the petcoke and coal roughness data is the magnitude of Ra (as well as Rt and Rz). The largest Ra value (not including the flake) for the petcoke series is 89% lower than that of the coal series, despite the larger particle size. Even with the flake roughness the no cooling Ra value is 50% lower than the same test using subbituminous coal. Considering the results of the particle size series (Figure 3-6) and the fact that the amount of deposition was similar for the two series (Table 5-2, Table 6-2) the petcoke particulate has a substantially different impact on roughness than the coal particulate. The differing sets of buttons could also have contributed to the disparity.

6.5 ESEM Analysis

The buttons for this test series were also analyzed using the ESEM. The sample preparation was the same as with the coal series except that the samples were cross-sectioned using a wire EDM machine instead of the water jet. Since the EDM can only cut metal, following the metal cross sectioning the TBC was cut using a diamond tipped water-cooled cutting machine.

The cross sectioned samples were again used to measure the thickness of deposit remaining on the surface (Figure 6-4). As with the coal impingement series, three images were taken of the cross sectioned sample: one at the bottom of the sample (closest to the combustor exit), one near the middle, and one at the top. Figure 6-5 shows a typical series of images taken from the 3.38 g/s cooling level sample.

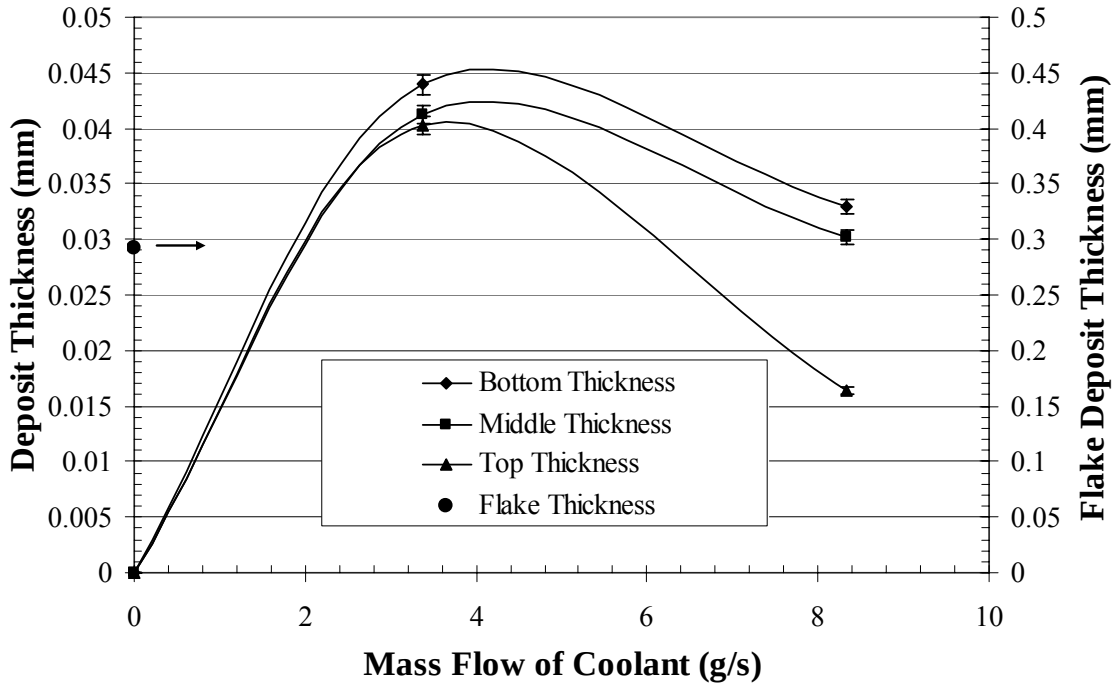

Figure 6-4: Remaining deposit thickness as a function of cooling level

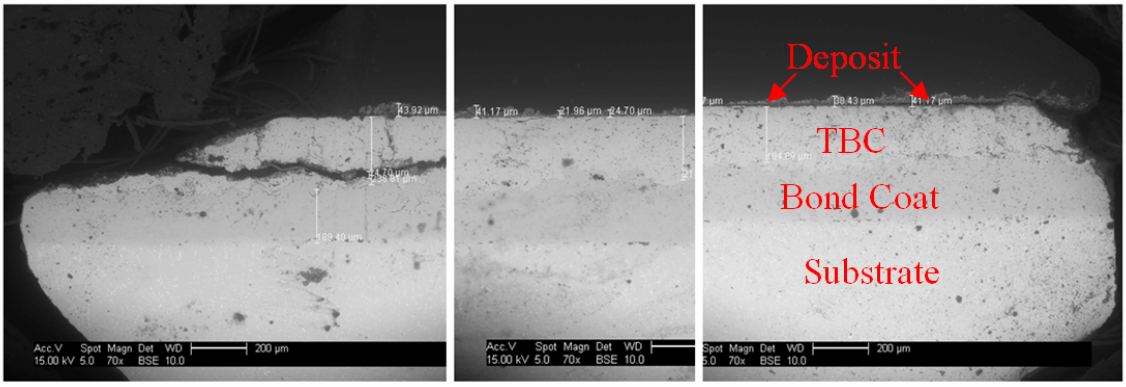

Figure 6-5: Typical image series of bottom (left), middle, and top (right) portions of 3.38 g/s coolant test sample

As seen in Figure 6-4, residual deposit thickness is uniform for the no cooling case (in fact there was no deposit present along the cross section). This is indicative of the large percentage of separated deposit for this case as noted in Table 6-2. As with the coal series, a flake was taken from the no cooling test and its thickness was measured using calipers. The averaged value is plotted in Figure 6-3 however its value was an order of magnitude greater than the other measurements and therefore plotted on the secondary axis as indicated. A similar trend to the coal series is seen with the petcoke series. The first amount of cooling (3.38 g/s) increased the residual deposit thickness fairly uniformly at all locations of the button because of the more tenacious nature of the deposit. At the highest cooling case the deposit thickness dropped off at all locations of the TBC, most notably at the top. Again the location from which the flake came is unknown; however, as with the coal series, the trend of decreased deposit thickness with increased cooling is apparent.

One difference between the coal and petcoke series is the much larger spatial variation of deposit thickness for the coal series with cooling (Figure 5-4). For the no

cooling case even after accounting for the flake thickness the petcoke deposit is 37% smaller than the no cooling test using coal. One possible explanation could be the petcokes' higher density which could produce similar deposition metrics (net deposit mass, deposition rate, net capture efficiency) to the coal series while having a thinner deposit.

X-ray spectroscopy was also conducted to determine the elemental constituents in the surface deposit, as well as the penetrating deposits. Figure 6-6 shows the elemental composition in weight percent compared with the ash. The surface deposits showed quite a different makeup from the ash. There was a significant increase in Fe and Ni while Al and Si showed large decreases. Na and Mg were not present in the surface deposit. The figure also clearly shows that the TBC studied is penetrated by almost all of the elements from the ash. The penetration of Na, Ca, and V are of particular concern since they are corrosive elements.

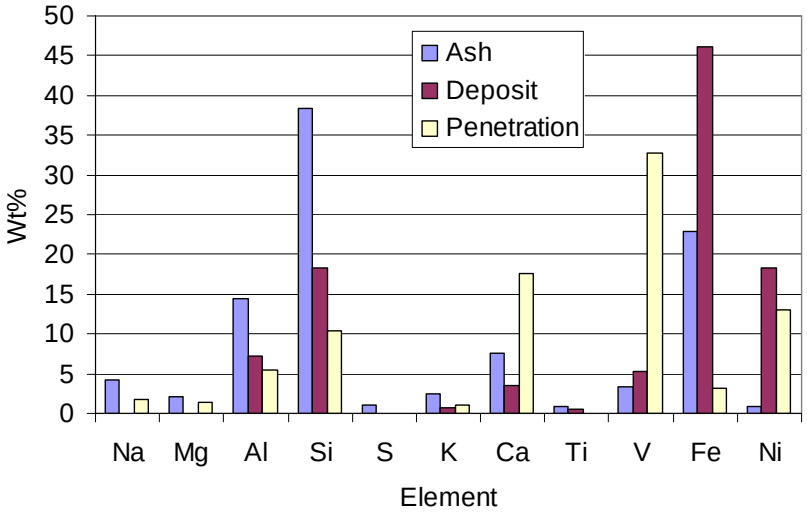

Figure 6-6: Elemental comparison of ash, deposit, and penetration for petcoke impingement cooling series

7 Conclusions and Recommendations

7.1 Conclusions

Four series of tests were performed in an accelerated deposition test facility to study the independent effects of particle size, gas temperature, and metal temperature on ash deposits from two candidate power turbine synfuels. Testing was conducted in the TADF by matching gas temperature, velocity, and net throughput of particulate out of the combustor with that experienced by a modern power turbine. Nominal combustor exit flow conditions were: Mach number of 0.25±0.021 and gas temperature of 1183±5°C. Testing with four different sizes of coal ash particles showed greater than double the deposition rate as particle mass mean diameter was increased from 3 to 16 μm. Roughness measurements were inconclusive as the large amounts of deposit separation could have biased the results.

In the second series of tests, different gas temperatures were studied while the facility maintained a constant exit velocity of 170±7m/s (Mach=0.23-0.26). Particle deposition rate was found to decrease with decreasing gas temperature. The threshold gas temperature for deposition was approximately 960°C for subbituminous coal. Roughness measurements showed a substantial decrease in roughness with decreased gas temperature. The one exception was the standard operating gas temperature (1183°C)

which experienced substantial deposit separation, and exhibited a much lower Ra than expected. Measuring the roughness of a flake taken from the standard operating gas temperature test substantiated the result of decreased roughness with decreased gas temperature.

Ground coal and petcoke ash particulates were used in the third and fourth test series with impingement cooling on the backside of the target button. Deposition rates decreased with increasing mass flow of coolant air, as expected. After measuring the roughness of a flake from the no cooling tests for both series the third test series provides some evidence of decreased roughness with increased cooling levels while the fourth test series shows strong evidence of this trend. Post exposure analyses of the third test series (environmental scanning electron microscopy and x-ray spectroscopy) show decreased deposit thickness with increased cooling. Post exposure analysis of the fourth test series showed similar trends, but the magnitudes were very different. Overall deposit thickness from the petcoke ash was much smaller than from the coal ash particulate. Petcoke ash deposit penetration also showed significantly more corrosive elements than from the coal ash particulate. Work is currently under way to study the effects of different TBC application techniques on deposition.

7.2 Accomplishments/Recommendations

This study accomplished numerous objectives. The TADF has been greatly improved as a research facility in terms of more stable and repeatable operation. This will greatly benefit future studies by eliminating undesirable variables so that those of interest can be studied. The new sample fixture has given the TADF a more realistic

engine operating condition. It also will allow easy transition to future film cooling studies without significant modifications.

The test series answered many questions of interest and generated some new ones that require future study. The particle size series established the need for proper functioning filtration systems in order to minimize deposition. As operators change to these alternate fuels, they will need to be more aware of how well the various filtration and gas cleanup systems are operating. An increase in routine maintenance could be required to keep larger particles from reaching the turbine section. It also improved upon the results from earlier studies performed in the TADF that used larger particles and whose relevance was called into question by some researchers. This test series established the fact that deposition will be a problem when burning ash bearing fuels even with the most state of the art clean up systems, as small particles can still produce significant deposits. As filtration and gas clean-up systems continue to advance this study suggests that deposition will continue to be reduced.

The gas temperature series established a threshold temperature for deposition from subbituminous coal ash particulate at approximately 960°C. Because engine operating temperatures continue to rise, in order to increase efficiency, this test series showed that deposition could become a larger problem. This test series also gives an indication of how deposition could affect more stages of the turbine depending on the temperature drop between each stage. The test series also showed that Eastern coal has a much higher threshold temperature for deposition. This result could have a significant impact on the decision of which type of coal to use depending on the engine operating temperature. This test series suggests that older engines that operate at lower

temperatures could begin using coal fuels and not see a significant problem with increased deposition.

The two impingement cooling series showed that deposition can be reduced (or even eliminated) by cooling. The amount of cooling required might be prohibitive; however any amount of cooling proved to be helpful in reducing deposition and protecting TBC blades. The two possible alternate fuels tested in this series, as well as the other two series, will provide valuable information to industry and allow them to make a more informed decision on which type of fuel to implement with a clear understanding of the implications in terms of deposition.

Some recommendations for improvement and future study are offered. Much of the testing revealed a need for a change in the TADF shutdown procedure. The immediate shutdown of the combustor was most likely the cause of the significant deposit separation and possibly spallation. A longer controlled shutdown procedure (similar to what happens with a real engine) would help eliminate this problem and perhaps allow for better roughness measurements to be taken using the profilometer. It will take the total test time to almost 12 hours, but will provide better results.

As previously mentioned an improved method of measuring the temperature drop across the button is needed. An optical method for measuring the backside temperature would provide improved results over the welded thermocouples and could be used to calculate the heat flux across the button. More thermocouples in the exiting coolant stream could also obtain a better mixed out temperature of the coolant and be used to calculate the heat flux. Better insulation of the fixture around where the button is held could also help to minimize the 3-D losses.

The steps used to prepare post-test buttons for analysis in the ESEM need to be reevaluated. In this study it is believed, based on visual inspection of the samples, that some of the damage to the TBC was caused by either the method used to cross-section the samples or the Bakelite process. The Bakelite process could be eliminated entirely as it only makes the polishing process more convenient.

A way to obtain even smaller particles could be investigated as a MMD of 3 μm is still larger than some researchers would like. Also of interest are higher operating temperatures; however this would require significant modifications to the TADF. More data should be collected for petcoke in order to make a better comparison to coal.

8 References

Bons, J.P., Taylor, R., McClain, S., and Rivir, R.B., 2001, "The Many Faces of Turbine Surface Roughness," ASME J. Turbomach., 123, No. 4, October 2001, pp. 739-748.

Bons, J.P., 2002, "St and C_f Augmentation for Real Turbine Roughness with Elevated Freestream Turbulence," Transactions of the ASME, vol. 124, OCT 2002, pp. 632-644.

Bons, J.P., Wammack, J.E., Crosby, J., Fletcher, D., and Fletcher, T.H., 2006, "Evolution of Surface Deposits on a High Pressure Turbine Blade, Part II: Convective Heat Transfer," presented at IGTI 2006 in Barcelona, Spain, May 2006, #GT2006-91257.

Bons, J.P., Crosby, J., Wammack, J.E., Bentley, B.I., and Fletcher, T.H., 2007, "High Pressure Turbine Deposition in Land-Based Gas Turbines with Various Synfuels," Journal of Engineering for Gas Turbines and Power, Jan 2007, pp. 135-143.

Borom, M. P., Johnson, C. A., and Peluso, L. A., 1996, "Role of environmental deposits and operating surface temperature in spallation of air plasma sprayed thermal barrier coatings," Surface and Coatings Technology 86-87, pp. 116-126.

Caguiat, D., 2002, “Rolls Royce/Allison 501-K Gas Turbine Anti-Fouling Compressor Coatings Evaluation,” presented at IGTI 2002 in Amsterdam, The Netherlands, June 2002, #GT2002-30261.

Ghenaiet, A., Elder, R. L., and Tan, S. C., 2001, “Particles and Trajectories through an Axial Fan and Performance Degradation due to Sand Ingestion,” ASME Paper No. 2001-GT-497, 2001.

Hamed, A., Tabakoff, W., Rivir, R.B., Das, K., and Arora, P., 2004, “Turbine Blade Surface Deterioration by Erosion,” Paper No. ASME-IGTI 2004-54328, June 2004.

Jensen, J. W., 2004, “The Development of an Accelerated Testing Facility for the Study of Deposits In Land-Based Gas Turbine Engines,” M.S. Thesis, Mechanical Engineering Department, Brigham Young University, Provo, Utah.

Jensen, J. W., Squire, S. W., and Bons, J. P., 2005, “Simulated Land-Based Turbine Deposits Generated in an Accelerated Deposition Facility,” ASME J. Turbomach., 127, pp. 462-470.

Kim, J., Dunn, M.G., and Baran, A.J. et al, 1993, “Deposition of Volcanic Materials in the Hot Sections of Two Gas Turbine Engines,” J. Engr. Gas Turbines & Power vol. 115, Jul 1993, pp 641-651.

Lu, H., 2006, “Experimental and Modeling Investigations of Biomass Particle Combustion,” PhD Dissertation, Chemical Engineering Department, Brigham Young University, Provo, Utah.

Sigal, A. and Danberg, J., 1990, "New Correlation of Roughness Density Effect on the Turbulent Boundary Layer," *AIAA Journal*, Vol. 28, No. 3, March 1990, pp. 554-556.

Smialek, J.L., Archer, F.A., and Garlick, R.G. in F.H. Froes et al. (eds.), 1992, "The Chemistry of Saudi Arabian Sand: A Deposition Problem on Helicopter Turbine Airfoils," Advances in Synthesis and Processes, SAMPE, 3, 1992, M92-M101.

Smoot, L.D., and Pratt, D.T, 1979, "Pulverized-Coal Combustion and Gasification," Plenum Press, New York, 1979.

Syverud, E., Brekke, O., and Bakken, L. E., 2005, "Axial Compressor Deterioration Caused By Saltwater Ingestion," presented at IGTI 2005 in Reno, Nevada, June 2005, #GT2005-68701.

Toriz, F.C., Thakker, A.B., and Gupta, S.K., J. ASME, "Thermal Barrier Coatings for Jet Engines" 88-GT-279, (1988), (presented at the Gas Turbine and Aeroengine Congress Amsterdam, The Netherlands, June 6-9, 1988).

Wammack, J. E., 2005, "Evolution of Turbine Blade Deposits in an Accelerated Deposition Facility: Roughness and Thermal Analysis," M.S. Thesis, Mechanical Engineering Department, Brigham Young University, Provo, Utah.

Wammack, J.E., Crosby, J., Fletcher, D., Bons, J.P., and Fletcher, T.H., 2006, "Evolution of Surface Deposits on a High Pressure Turbine Blade, Part I: Physical Characteristics," presented at IGTI 2006 in Barcelona, Spain, May 2006, #GT2006-91246.

Wenglarz, R.A., and Fox, R.G. Jr., 1990, “Physical Aspects of Deposition From Coal-Water Fuels Under Gas Turbine Conditions”, Journal of Engineering for Gas Turbines and Power, Jan 1990, pp9-14.

Wenglarz, R.A., and Wright, I.G., 2002, “Alternate Fuels for Land-Based Turbines,” published in proceedings of the “Workshop on Materials and Practices to Improve Resistance to Fuel Derived Environmental Damage in Land-and Sea-Based Turbines,” October 22-24, 2002, Colorado School of Mines, Golden, Colorado.

Appendix A. Uncertainty Analysis

An uncertainty analysis was conducted on the mass flow and Mach number of the TADF. The choked flow mass flow equation was used.

$$\dot{m} = \frac{C_D A P}{\sqrt{RT}} \sqrt{\gamma} \left(\frac{2}{\gamma + 1} \right)^{\frac{\gamma+1}{2(\gamma-1)}} \tag{A.1}$$

$$u_{\dot{m}} = \left[\left(\frac{\partial \dot{m}}{\partial C_D} u_{C_D} \right)^2 + \left(\frac{\partial \dot{m}}{\partial A} u_A \right)^2 + \left(\frac{\partial \dot{m}}{\partial P} u_P \right)^2 + \left(\frac{\partial \dot{m}}{\partial T} u_T \right)^2 \right]^{0.5} \tag{A.2}$$

$$u_{\dot{m}} = \left[\left(\frac{AP}{\sqrt{RT}} C u_{C_D} \right)^2 + \left(\frac{C_D P}{\sqrt{RT}} C u_A \right)^2 + \left(\frac{C_D A}{\sqrt{RT}} C u_P \right)^2 + \left(-\frac{C_D A P}{2\sqrt{R} T^{3/2}} C u_T \right)^2 \right]^{0.5} \tag{A.3}$$

$$\text{Where } C = \sqrt{\gamma} \left(\frac{2}{\gamma + 1} \right)^{\frac{\gamma+1}{2(\gamma-1)}} \tag{A.4}$$

The uncertainty in pressure (P) came from the pressure transducer specification which was listed as 0.25% of full scale (200 psi) which is 0.5 psi or 3447.38 Pa. Uncertainty in temperature (T) was specified as 2.2 K from the manufacturer. Uncertainty in area (A) came from the following analysis.

$$A = \frac{\pi D^2}{4} \tag{A.5}$$

$$u_A = \left[\left(\frac{\partial A}{\partial D} u_D \right)^2 \right]^{0.5} \tag{A.6}$$

$$u_A = \frac{\pi D}{2} u_D \tag{A.7}$$

Estimating the uncertainty in diameter as $1.016e^{-4}$ m (0.004 in) and inserting the appropriate values into A.7:

$$u_A = 8.958e^{-7} m^2$$

Uncertainty in C_D was obtained from a calibration curve fit uncertainty analysis (Figure A - 1, Table A - 1). Inserting all the appropriate values into equation A.3 gave an uncertainty in combustor mass flow of $1.003e^{-3}$ kg/s which was approximately 4.7% of the total mass flow.

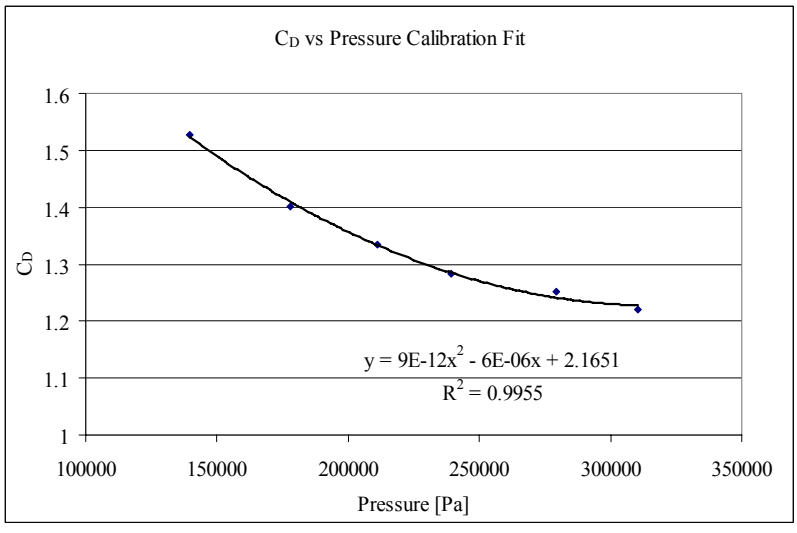

Figure A - 1: Mass flow calibration curve fit

Table A - 1: Calibration curve fit uncertainty analysis

Pressure Transducer [psi]	Pressure Transducer [Pa]	Temperature [°C]	Mdot from Meter [kg/s]	CD Measured	CD Curve Fit	Diff Squared
20.25	139618.58	18.2	0.0125	1.5278	1.5227	2.562E-05
25.8	177884.42	18.2	0.0146	1.4006	1.4097	8.3E-05
30.6	210979.19	18.2	0.0165	1.3345	1.3338	5.562E-07
34.7	239247.65	18.2	0.018	1.2838	1.2850	1.445E-06
40.5	279237.17	18.2	0.0205	1.2528	1.2414	0.0001299
45	310263.52	18.2	0.0222	1.2210	1.2279	4.75E-05
			avg	**1.3367**	**sum**	**0.000288**
					Syx	**0.009799**
			meter error	0.0173	**95% uncertainty**	**0.025192**
			avg error	**0.023125616**	**avg flowmeter error**	0.0231256
					uncertainty in C_D	**0.034197**

The exact same procedure was used to find the uncertainty in the highest and lowest coolant mass flows tested. For the highest mass flow the uncertainty was found to be approximately 0.49 g/s or 5.8% of the total coolant flow. For the lowest mass flow the uncertainty was approximately 0.48 g/s, however this represented 38% of the total coolant flow.

Uncertainty in the Mach number of the TADF was calculated using the Mach number equation through the following analysis.

$$M = \frac{V}{a} \tag{A.8}$$

$$u_M = \left[\left(\frac{\partial M}{\partial V} u_V \right)^2 + \left(\frac{\partial M}{\partial a} u_a \right)^2 \right]^{0.5} \tag{A.9}$$

$$u_M = \left[\left(\frac{1}{\sqrt{\gamma RT}} u_V \right)^2 + \left(-\frac{V}{2\sqrt{\gamma R}\left(T^{3/2}\right)} u_T \right)^2 + \left(-\frac{V}{2\sqrt{RT}\left(\gamma^{3/2}\right)} u_\gamma \right)^2 \right]^{0.5} \quad \text{(A.10)}$$

Uncertainty in T was used previously and came from the manufacturer. Uncertainty in gamma was estimated at 0.05 and uncertainty in velocity was found from the following analysis.

$$V = \frac{\dot{m}}{\rho A} \quad \text{(A.11)}$$

$$u_V = \left[\left(\frac{\partial V}{\partial \dot{m}} u_{\dot{m}} \right)^2 + \left(\frac{\partial V}{\partial \rho} u_\rho \right)^2 + \left(\frac{\partial V}{\partial A} u_A \right)^2 \right]^{0.5} \quad \text{(A.12)}$$

$$u_V = \left[\left(\frac{1}{\rho A} u_{\dot{m}} \right)^2 + \left(-\frac{\dot{m}}{\rho^2 A} u_\rho \right)^2 + \left(-\frac{\dot{m}}{\rho A^2} u_A \right)^2 \right]^{0.5} \quad \text{(A.13)}$$

Uncertainty in mass flow has already been found. Uncertainty in area was found using equation A.7 where D was the diameter of the equilibration tube and was found to be equal to $4.252e^{-6}$ m^2. Uncertainty in density was found using the following analysis.

$$\rho = \frac{P}{RT} \quad \text{(A.14)}$$

$$u_\rho = \left[\left(\frac{\partial \rho}{\partial P} u_P \right)^2 + \left(\frac{\partial \rho}{\partial T} u_T \right)^2 \right]^{0.5} \tag{A.15}$$

$$u_\rho = \left[\left(\frac{1}{RT} u_P \right)^2 + \left(-\frac{P}{RT^2} u_T \right)^2 \right]^{0.5} \tag{A.16}$$

Uncertainty in pressure was estimated to be 0.1 psi (689.5 Pa) and the uncertainty in temperature was the same as used previously. Using equation A.16 and the appropriate values uncertainty in density was found to be $2.172e^{-3}$ kg/m^3. Substituting the appropriate values into equation A.13 the uncertainty in velocity was found to be 6.28 m/s. This value was substituted with all other values found from the above analyses into equation A.10 to give an uncertainty in Mach number of 0.021 or 8.5% of the TADF operating Mach number.

An uncertainty analysis was conducted on the heat flux calculations described in Chapter 2.4. Uncertainties were estimated for the thermal conductivities and thicknesses of the substrate and TBC layers. Frontside temperature as well as backside temperature uncertainty was estimated. The partial derivative method for evaluating uncertainty was used on both the conductive heat flux calculation, and coolant flux (Eq 2.9) equation described in Chapter 2.4. The error bars in Figure 2-13 show the uncertainties calculated. For the conductive flux, uncertainty was approximately 15% at all coolant levels. For the coolant flux uncertainty was between 17-19% for the three highest coolant flows, but was approximately 40% for the lowest coolant flow rate. The large uncertainty in the coolant mass flow rate (at low mass flows) caused the large uncertainty at the 1.26 g/s flow rate.

The particle size measurements from the coulter counter were also assessed for uncertainty. Precision uncertainty for the coulter counter was unavailable. Instead the standard deviation of the tests used to find the average MMD for the different particle sizes was used as an estimate of uncertainty. The small and medium size subbituminous coal had the most tests performed using the coulter counter. Results were presented in Chapter 2.5. Because the large and unground coal particles, as well as the petcoke particles, did not have many tests performed, they have slightly larger uncertainties.

For the ash elemental composition, as well as the deposit elemental composition in the coal and petcoke impingement cooling series results, the uncertainty in the x-ray spectroscopy measurements was assessed. According to the ESEM technician, Mike Standing, for a polished sample of homogenous material without calibration using a standard, the results from the ESEM have a relative error of ±10%.

An uncertainty analysis was conducted on the particle loadings of all tests. Using the uncertainty in air mass flow calculated previously, the uncertainty in mass measurements mentioned in Chapter 2.3, as well as estimating the uncertainty in test time as one minute yielded the uncertainties cited in the various Chapters.

An uncertainty analysis was also conducted on all of the deposition metrics (deposition rate, net capture efficiency, and separated deposit percentage) using the partial derivative method on the equations used to calculate them. The ranges of uncertainties are reported with the various results in Chapters 3-6.

The profilometer uncertainty was evaluated from the following analysis. The precision uncertainty was found by calibrating against a standard roughness pattern and was found to be 0.4353 μm. Only Ra was able to be calibrated, but the precision

uncertainty was applied to Rt, and Rz as well. For the various test series, the standard deviation for the 4 (or 6) traces averaged was multiplied by the t estimator from a Student-t distribution for 95% confidence. The uncertainty was obtained by taking the root mean square of these two values. The results are included in the roughness figures for the various test series.

Deposit thickness uncertainty was evaluated by looking at the precision uncertainty of the ESEM measurements. According to the ESEM technician, Mike Standing, the ESEM was calibrated four years ago when it was first installed. The calibration involved looking at a grid of known dimensions at a relatively low magnification of 1000x. The results are estimated to be accurate to within 2%.